Title

Tidal heating in icy satellite oceans

Journal

Icarus, 229

ISSN

0019-1035

Authors

Chen, EMA
Nimmo, F
Glatzmaier, GA

Publication Date

2014-02-01

DOI

10.1016/j.icarus.2013.10.024

Peer reviewed

Icarus 229 (2014) 11–30

Contents lists available at ScienceDirect

Icarus

journal homepage: www.elsevier.com/locate/icarus

Tidal heating in icy satellite oceans

E.M.A. Chen, F. Nimmo *, G.A. Glatzmaier

Dept. Earth and Planetary Sciences, University of California, Santa Cruz, 1156 High St., Santa Cruz, CA 95064, USA

ARTICLE INFO

Article history:
Received 14 May 2013
Revised 21 October 2013
Accepted 22 October 2013
Available online 30 October 2013

Keywords:
Satellites, dynamics
Tides, solid body
Jupiter, satellites
Saturn, satellites
Triton

ABSTRACT

Tidal heating plays a significant role in the evolution of many satellites in the outer Solar System; however, it is unclear whether tidal dissipation in a global liquid ocean can represent a significant additional heat source. Tyler (Tyler, R.H. [2008]. Nature 456, 770-772; Tyler, R.H. [2009]. Geophys. Res. Lett. 36, doi:10.1029/2009GL038300) suggested that obliquity tides could drive large-scale flow in the oceans of Europa and Enceladus, leading to significant heating. A critical unknown in this previous work is what the tidal quality factor, Q, of such an ocean should be. The corresponding tidal dissipation spans orders of magnitude depending on the value of Q assumed.

To address this issue we adopt an approach employed in terrestrial ocean modeling, where a significant portion of tidal dissipation arises due to bottom drag, with the drag coefficient O (0.001) being relatively well-established. From numerical solutions to the shallow-water equations including nonlinear bottom drag, we obtain scalings for the equivalent value of Q as a function of this drag coefficient. In addition, we provide new scaling relations appropriate for the inclusion of ocean tidal heating in thermal–orbital evolution models. Our approach is appropriate for situations in which the ocean bottom topography is much smaller than the ocean thickness.

Using these novel scalings, we calculate the ocean contribution to the overall thermal energy budgets for many of the outer Solar System satellites. Although uncertainties such as ocean thickness and satellite obliquity remain, we find that for most satellites it is unlikely that ocean tidal dissipation is important when compared to either radiogenic or solid-body tidal heating. Of known satellites, Triton is the most likely icy satellite to have ocean tidal heating play a role in its present day thermal budget and long-term thermal evolution.

1. Introduction

Tidal heating influences the present-day behavior of some planetary bodies, such as Io (Peale et al., 1979) and Enceladus (Spencer et al., 2006; Howett et al., 2011). It probably also played a role at earlier times elsewhere, including Europa (Hussmann and Spohn, 2004), Ganymede (Showman et al., 1997), Triton (Jankowski et al., 1989), and the Moon (Garrick-Bethell et al., 2010), and may be important in some super-Earth exoplanets (Henning et al., 2009).

For solid bodies, the effects of tides and their associated dissipation are typically calculated assuming a viscoelastic rheology, such as Maxwell, Andrade or Burgers (e.g. Ross and Schubert (1989); Tobie et al. (2005); Efroimsky and Williams (2009); Castillo-Rogez et al. (2011); Nimmo et al. (2012)), though other processes (such as frictional heating, e.g. Nimmo and Gaidos (2002)) may also play a role. For primarily fluid bodies, such as giant planets, a significant component of dissipation is likely to be due to the breaking of internal gravity waves (Ogilvie and Lin, 2004). Lastly, fluid layers on or within solid bodies may also be a source of dissipation. On the Earth it is well-known that tidal dissipation occurs mainly in the oceans (Munk and MacDonald, 1960; Egbert and Ray, 2000; Ray et al., 2001). Global subsurface oceans are thought to occur on at least Europa, Ganymede, Callisto, Titan and perhaps Enceladus (Khurana et al., 1998; Kivelson et al., 2002; Bills and Nimmo, 2011; Iess et al., 2012; Postberg et al., 2011); our focus in this paper is to examine tidal dissipation within such oceans.

In a prescient paper, Ross and Schubert (1989) discussed the possibility of tidal heating on Enceladus arising from turbulent dissipation in a subsurface ocean. More recently, Tyler (2011) expanded an analysis initially developed by Longuet-Higgins (1968) to investigate energy dissipation in tidally-driven satellite oceans. In Tyler (2011), a key free parameter is the linear drag constant α, which can be related to a tidal quality factor Q. It is worth noting that the value of α or Q is *a priori* very poorly known and the total energy dissipation scales linearly with the model's prescribed value.

In this paper, we follow an analysis similar to that of Tyler (2011). However, we depart from his approach in two important respects. First, we provide an estimate for Q using an approach and parameter values developed in studies of the Earth's oceans.

* Corresponding author.
E-mail address: fnimmo@es.ucsc.edu (F. Nimmo).

0019-1035/$ - see front matter © 2013 Elsevier Inc. All rights reserved.
http://dx.doi.org/10.1016/j.icarus.2013.10.024

Second, we present approximate scaling relationships which allow fluid dissipation to be calculated in a manner analogous to the well-known equations for solid body dissipation (e.g. Segatz et al. (1988); Ross and Schubert (1989); Wisdom (2008)). This will facilitate investigation of long-term satellite evolution, in which the thermal and orbital histories are coupled (e.g. Ojakangas and Stevenson (1989); Hussmann and Spohn (2004); Bland et al. (2009); Meyer et al. (2010); Zhang and Nimmo (2012)).

The rest of this paper is organized as follows. Section 2 reviews the shallow water equations appropriate for flow in global fluid layers on a rotating spherical shell. For clarity, we summarize a semi-analytic solution to these equations, similar to that adopted by Longuet-Higgins (1968) and Tyler (2011), and in addition, explicitly present the method and equations used to calculate quantities such as the average kinetic energy and energy dissipation. Section 3 simplifies this system and carries out an analytical study of the response of a shallow global ocean to tidal forcing, building on the method presented in Section 2. This novel analysis derives approximate scaling relationships for ocean tidal flow and the resulting dissipation under typical icy satellite parameters. The algebra involved can be tedious; to aid clarity, many details have been relegated to Appendices E and F, while Table 4 summarizes the key results. The advantage of these relationships is that they retain the fundamental physical effects while being somewhat simpler to implement than the method presented in Section 2. The results of Section 3 are expressed in terms of an unknown effective (presumably turbulent) viscosity. In Section 4, we present an estimate for this viscosity using a numerical technique based on analogy to frictional ocean dissipation on Earth. We discuss the applications and implications of these results in Section 5. In particular, ocean dissipation is unlikely to be a significant heat source unless the orbital eccentricity is very small; Triton is thus the most likely candidate for a satellite in which ocean tidal dissipation is significant.

2. Ocean tidal dissipation

Here we briefly review the equations of motion for a shallow global satellite ocean. These equations are equivalent to Eqs. (3) and (4) presented in Tyler (2011); we present fully dimensional equations and explicitly expand these equations for the solutions to unknown spherical harmonic coefficients.

The forced, dissipative, shallow water equations on a rotating sphere are (cf. Longuet-Higgins (1968) Eqs. (13.1)–(13.3) or Tyler (2011) Eqs. (3) and (4), noting the sign difference in the tidal potential term)

$$\frac{\partial \vec{u}}{\partial t} + 2\Omega \cos\theta \hat{r} \times \vec{u} = -g\vec{\nabla}\eta - \vec{\nabla}U - \alpha\vec{u} + \nu\nabla^2\vec{u} \tag{1}$$

and

$$\frac{\partial \eta}{\partial t} + h\vec{\nabla}\cdot\vec{u} = 0, \tag{2}$$

where $\vec{u}$ is the radially-averaged, horizontal velocity vector, Ω is the constant rotation rate, $\hat{r}$ is the unit vector in the radial direction, g is the surface gravity, η is the vertical displacement of the surface, and h is the constant ocean depth. The dissipation can be represented as either a linear process with a linear coefficient α or a Navier–Stokes type viscosity with a viscous diffusivity of ν. We assume no radial gradients in our shallow-water model such that the Laplacian operator, ∇^2, has no radial contributions and thus, ν is an effective horizontal diffusivity. U represents the forcing potential due to tides, either eccentricity- or obliquity-related. Eqs. (1) and (2) are valid for incompressible flow under the assumptions that the thickness of the fluid layer is much smaller than the radius of the body ($h \ll R$), the vertical displacement is much smaller than the layer thickness ($\eta \ll h$) and fluid properties are constant (e.g. α and ν). These equations ignore ocean stratification, and thus do not include the effects of internal tides. In addition, they do not include overlying ice shell rigidity, though this effect should be small (Matsuyama, 2012).

2.1. Tidal potentials

For synchronously rotating satellites, such as the regular satellites of Jupiter and Saturn, we are concerned with the ocean flow driven by the eccentricity of the orbit and the obliquity, the tilt of the rotational axis relative to the orbital axis. The forcing tidal potentials can be derived by assuming the planet is a point mass and calculating the resulting gravitational potential at every point on the satellite (cf. Kaula (1964); Murray and Dermott (1999)).

2.1.1. Obliquity tides

The obliquity tidal potential at a point of colatitude θ and longitude ϕ on a synchronously rotating satellite with small obliquity θ_0 (in radians) is a standing wave and can be written as the sum of an eastward and a westward propagating potential (cf. Tyler (2011) Eq. (34))

$$U_{obl} = \frac{-3}{2}\Omega^2 R^2 \theta_0 \sin\theta\cos\theta(\cos(\phi - \Omega t) + \cos(\phi + \Omega t)). \tag{3}$$

We define Laplace spherical harmonics of degree l and order m, Y_l^m, as

$$Y_l^m(\theta,\phi) \equiv \sqrt{\frac{(2l+1)}{4\pi}\frac{(l-m)!}{(l+m)!}}P_l^m(\cos\theta)e^{im\phi} \tag{4}$$

employing a Condon–Shortley phase factor of $(-1)^m$ for $m > 0$. These spherical harmonics are orthogonal under

$$\int_0^{2\pi}\int_0^{\pi} Y_l^m Y_{l'}^{m'*} \sin\theta d\theta d\phi = \delta_{l,l'}\delta_{m,m'} \tag{5}$$

where * denotes the complex conjugate and δ is the Kronecker delta.

The obliquity tidal potential thus can be expressed in spherical harmonics as a westward propagating potential $U_{obl,W}$,

$$\begin{aligned} U_{obl,W} &= \frac{3}{2}\sqrt{\frac{2\pi}{15}}\Omega^2 R^2\theta_0(e^{i\Omega t}Y_2^1 - e^{-i\Omega t}Y_2^{-1}) \\ &= 2\left(\frac{3}{2}\sqrt{\frac{2\pi}{15}}\Omega^2 R^2\theta_0\right)\Re(e^{i\Omega t}Y_2^1) \equiv 2U_{2,W}^1\Re\left(e^{i\Omega t}Y_2^1\right), \end{aligned} \tag{6}$$

and a symmetric eastward propagating potential $U_{obl,E}$ for which the $e^{i\Omega t}$ term is replaced by $e^{-i\Omega t}$ and $U_{2,E}^1 = U_{2,W}^1$.

2.1.2. Eccentricity tides

The eccentricity tidal potential can be expressed as (Kaula, 1964) (cf. Tyler (2011) Eq. (35))

$$\begin{aligned} U_{ecc} = \frac{-3}{4}\Omega^2 R^2 e[&-(3\cos^2\theta - 1)\cos\Omega t + \sin^2\theta(3 \\ &\times \cos 2\phi\cos\Omega t + 4\sin 2\phi\sin\Omega t)]. \end{aligned} \tag{7}$$

For the subsequent analysis, the eccentricity tidal potential can be split into three separate components. There is an axisymmetric component, $U_{ecc,rad}$, (Tyler (2011) calls this the "radial" component)

$$\begin{aligned} U_{ecc,rad} &= \left(3\sqrt{\frac{\pi}{5}}\Omega^2 R^2 e\cos\Omega t\right)Y_2^0 \\ &= \frac{1}{2}\left(3\sqrt{\frac{\pi}{5}}\Omega^2 R^2 e\right)(e^{i\Omega t} + e^{-i\Omega t})Y_2^0 \equiv U_2^0(e^{i\Omega t} + e^{-i\Omega t})Y_2^0 \end{aligned} \tag{8}$$

There is also an asymmetric librational component, $U_{ecc,lib}$, that can be split into a westward propagating potential

$$U_{ecc,lib,W} = \left(\frac{3}{4}\sqrt{\frac{2\pi}{15}}\Omega^2 R^2 e\right)\left(e^{i\Omega t}Y_2^2 + e^{-i\Omega t}Y_2^{-2}\right) = 2\left(\frac{3}{4}\sqrt{\frac{2\pi}{15}}\Omega^2 R^2 e\right)\Re\left(e^{i\Omega t}Y_2^2\right) \equiv 2U_{2,W}^2\Re\left(e^{i\Omega t}Y_2^2\right) \quad (9)$$

and an eastward propagating potential

$$U_{ecc,lib,E} = \left(\frac{-21}{4}\sqrt{\frac{2\pi}{15}}\Omega^2 R^2 e\right)\left(e^{-i\Omega t}Y_2^2 + e^{i\Omega t}Y_2^{-2}\right) = 2\left(\frac{-21}{4}\sqrt{\frac{2\pi}{15}}\Omega^2 R^2 e\right)\Re\left(e^{-i\Omega t}Y_2^2\right) \equiv 2U_{2,E}^2\Re\left(e^{-i\Omega t}Y_2^2\right). \quad (10)$$

2.2. Semi-analytic method of solution

The horizontal velocity can be expressed using a Helmholtz decomposition as the sum of the gradient of a scalar potential Φ and the curl of a streamfunction $\Psi\hat{r}$ where (cf. Tyler (2011) Eq. (5))

$$\vec{u} = \vec{\nabla}\Phi + \vec{\nabla}\times\Psi\hat{r} = u_\theta\hat{\theta} + u_\phi\hat{\phi}, \quad (11)$$

with the components of velocity given by

$$u_\theta = \frac{1}{R}\frac{\partial\Phi}{\partial\theta} + \frac{1}{R\sin\theta}\frac{\partial\Psi}{\partial\phi} \quad (12)$$

and

$$u_\phi = \frac{1}{R\sin\theta}\frac{\partial\Phi}{\partial\phi} - \frac{1}{R}\frac{\partial\Psi}{\partial\theta}. \quad (13)$$

The divergence and radial component of the curl of (11) are

$$\vec{\nabla}\cdot\vec{u} = \nabla^2\Phi, \quad (14)$$

$$\hat{r}\cdot(\vec{\nabla}\times\vec{u}) = -\nabla^2\Psi. \quad (15)$$

Taking the divergence of the momentum Eq. (1) and making the substitution from (14) results in

$$\left[\left(\frac{\partial}{\partial t} + \alpha - \nu\nabla^2\right)\nabla^2 + \frac{2\Omega}{R^2}\frac{\partial}{\partial\phi}\right]\Phi + 2\Omega\left[\cos\theta\nabla^2 - \frac{\sin\theta}{R^2}\frac{\partial}{\partial\theta}\right]\Psi = -g\nabla^2\eta - \nabla^2 U. \quad (16)$$

Similarly, the radial component of the curl of the momentum equation with the substitution (15) is

$$\left[\left(\frac{\partial}{\partial t} + \alpha - \nu\nabla^2\right)\nabla^2 + \frac{2\Omega}{R^2}\frac{\partial}{\partial\phi}\right]\Psi - 2\Omega\left[\cos\theta\nabla^2 - \frac{\sin\theta}{R^2}\frac{\partial}{\partial\theta}\right]\Phi = 0. \quad (17)$$

Eqs. (16) and (17) are equivalent to Eq. (3.7) of Longuet-Higgins (1968), with the dissipative terms added. Eqs. (16) and (17) are also equivalent to Eqs. (12) and (13) of Tyler (2011) if one ignores the residual terms (R_1 and R_2) and does not make the substitution for η using the continuity equation (see (18) below).

Substituting (14) into (2), the surface displacement is dependent only on Φ,

$$\frac{\partial\eta}{\partial t} + h\nabla^2\Phi = 0. \quad (18)$$

For the response to a westward propagating tidal potential, we seek wave solutions of the form

$$\Psi(\theta,\phi,t) = \sum_{l=1}^{\infty}\sum_{m=1}^{l}\left[\Psi_l^m e^{i\Omega t}Y_l^m + \Psi_l^{-m}e^{-i\Omega t}Y_l^{-m}\right] = 2\Re\left(\sum_{l=1}^{\infty}\sum_{m=1}^{l}\left[\Psi_l^m e^{i\Omega t}Y_l^m\right]\right), \quad (19)$$

with equivalent expansions for Φ and η. Here the coefficients Ψ_l^m (and their equivalents Φ_l^m, and η_l^m) are complex, thereby permitting a phase lag between the tidal forcing and the response. The response frequency is assumed to be the same as the forcing frequency.

Using Eq. (18) and the wave solutions for Ψ (19) and its equivalents, we have

$$\eta_l^m = -i\frac{h}{R^2\Omega}l(l+1)\Phi_l^m. \quad (20)$$

Plugging these wave solutions into Eqs. (16) and (17) and projecting the equations onto each spherical harmonic, we obtain equations describing solutions for the coefficients Ψ_l^m and Φ_l^m that are coupled in l but separable in m,

$$\left[i\Omega + \alpha + \frac{\nu l(l+1)}{R^2} - \frac{2\Omega i m}{l(l+1)}\right]\Psi_l^m - 2\Omega\left[\frac{l-1}{l}C_l^m\Phi_{l-1}^m + \frac{l+2}{l+1}C_{l+1}^m\Phi_{l+1}^m\right] = 0, \quad (21)$$

$$\left[i\Omega + \alpha + \frac{\nu l(l+1)}{R^2} - \frac{2\Omega i m}{l(l+1)} - \frac{igh l(l+1)}{\Omega R^2}\right]\Phi_l^m + 2\Omega\left[\frac{l-1}{l}C_l^m\Psi_{l-1}^m + \frac{l+2}{l+1}C_{l+1}^m\Psi_{l+1}^m\right] = \left\{-U_{2,W}^1\delta_{l,2}\delta_{m,1}, -U_{2,W}^2\delta_{l,2}\delta_{m,2}\right\} \quad (22)$$

with the term on the right hand side of (22) corresponding to the forcing potential of interest, either westward obliquity or westward librational eccentricity. The constants C_l^m are due to differential operators of the spherical harmonics, and these are given by

$$C_l^m = \left(\frac{(l+m)(l-m)}{(2l+1)(2l-1)}\right)^{1/2}. \quad (23)$$

Eqs. (21) and (22) are effectively Eq. (3.19) of Longuet-Higgins (1968) with correction of the sign inconsistencies described in Appendix A.1 of Tyler (2011). The differences in the constants between the equations presented here and those of Longuet-Higgins (1968) and Tyler (2011) are primarily due to the use of normalized spherical harmonics throughout this work and a difference in the sign of the tidal potentials. For helpful relations, similar to (3.17) and (3.18) of Longuet-Higgins (1968), we refer the reader to Appendix A. The linear system defined by Eqs. (21) and (22) can be easily solved numerically for the coupled coefficients Φ_l^m and Ψ_l^m, repeating for each potential of interest. While the series is infinite, typically the coefficients drop off rapidly with increasing l (Fig. 1). We exploit this fact in Section 3 to derive analytical scalings that reduce the complexity of implementing ocean tidal effects in thermal evolution models.

A similar projection can be obtained for the eastward forcing potentials by changing the direction of the response in (19) and its equivalents (see details in Appendix B). Additionally, in (19) we have neglected the contributions from the radial component of the eccentricity tide ($m = 0$). These coefficients must be real and thus, different wave solutions are required. We present the solution method explicitly in Appendix C. We have presented the westward response because for satellite oceans the dominant response is likely to be that to the westward propagating component of the obliquity tide (Tyler, 2008); for further details, we direct the reader to Section 3.1.

Given the spherical harmonics coefficients for Φ and Ψ, the average kinetic energy and energy dissipation can then be calculated. It can be shown (see details in Appendix D) that the kinetic energy averaged over the satellite surface and the orbital period is given by:

$$E_{tot,avg} = \rho h\left[\sum_{l=1}^{\infty}l(l+1)\left(|\Phi_{l,W}^0|^2 + |\Psi_{l,W}^0|^2\right) + \sum_{l=1}^{\infty}\sum_{m=1}^{l}l(l+1)\left(|\Phi_{l,W}^m|^2 + |\Phi_{l,E}^m|^2 + |\Psi_{l,W}^m|^2 + |\Psi_{l,E}^m|^2\right)\right]. \quad (24)$$

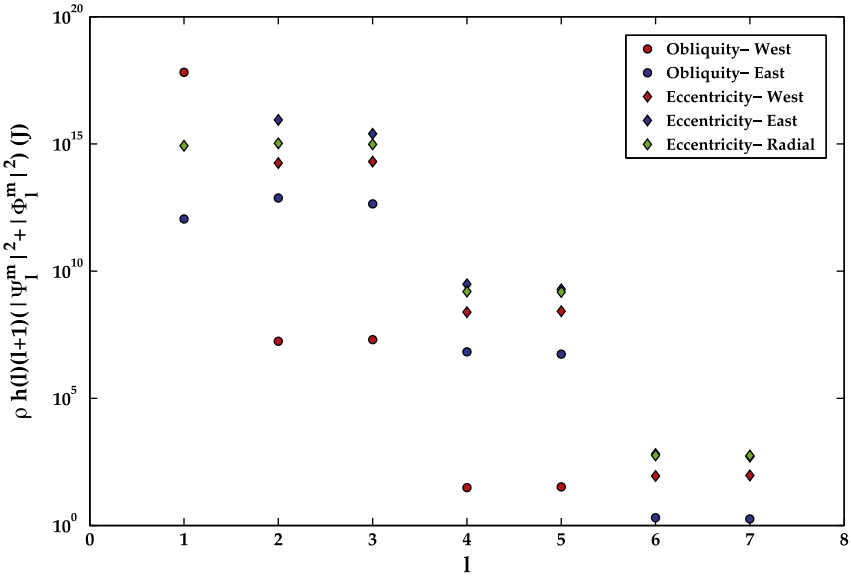

Fig. 1. Power spectrum with varying spherical harmonic degree l of the full semi-analytic solution described in Section 2.2 using parameters relevant to an ocean on Europa (Tables 1 and 2), here with a viscosity of $\nu = 1.0 \times 10^2$ m^2/s for both the obliquity and eccentricity tides. The response of each tidal component is separated. Note the significant separation between degrees 1 and 2 in the case of the westward obliquity response and degrees 3 and 4 for all other tidal components, justifying the scaling arguments presented in Section 3 and Appendices E and F.

The corresponding average flow speed $\bar{u}$ is then given by

$$\bar{u} = \left(\frac{E_{tot,avg}}{2\pi R^2 h\rho}\right)^{1/2}. \tag{25}$$

The energy dissipation rate similarly averaged (and taken to be positive) is

$$\dot{E}_{lin,avg} = 2\alpha E_{tot,avg} = 2\alpha\rho h\left[\sum_{l=1}^{\infty} l(l+1)\left(|\Phi^0_{l,W}|^2 + |\Psi^0_{l,W}|^2\right) + \sum_{l=1}^{\infty}\sum_{m=1}^{l} l(l+1)\left(|\Phi^m_{l,W}|^2 + |\Phi^m_{l,E}|^2 + |\Psi^m_{l,W}|^2 + |\Psi^m_{l,E}|^2\right)\right], \tag{26}$$

for linear dissipation and

$$\dot{E}_{NS,avg} = \frac{2\rho h\nu}{R^2}\left[\sum_{l=1}^{\infty} l^2(l+1)^2\left(|\Phi^0_{l,W}|^2 + |\Psi^0_{l,W}|^2\right) + \sum_{l=1}^{\infty}\sum_{m=1}^{l} l^2(l+1)^2\left(|\Phi^m_{l,W}|^2 + |\Phi^m_{l,E}|^2 + |\Psi^m_{l,W}|^2 + |\Psi^m_{l,E}|^2\right)\right]. \tag{27}$$

for Navier–Stokes type dissipation.

An alternative method of thinking about tidal dissipation is that in the time- and spatially-averaged sense it is equivalent to the work done by the tides. It can be shown that this work is related to distorting the surface (see details in Appendix D.2.2):

$$\dot{E}_{avg} = -2(2)(3)\rho h\left[U^0_2 \Re\left(\Phi^0_{2,W}\right) + \sum_{m=1}^{2}\left(U^m_{2,W}\Re(\Phi^m_{2,W}) + U^m_{2,E}\Re\left(\Phi^m_{2,E}\right)\right)\right]. \tag{28}$$

Note that dissipation depends only on the real part of Φ and is independent of Ψ. Two physical consequences follow immediately. First, situations in which there is no surface displacement ($\eta = \Phi = 0$ as in Tyler (2008)) will result in no dissipation. Second, while the amount of kinetic energy depends on the magnitude of Φ (see (24)), the energy dissipation rate depends on only the real component of Φ, and thus is sensitive to the phase lag between the tidal forcing and the fluid response, similar to viscoelastic tidal dissipation in solid bodies (Kaula, 1964; Peale and Cassen, 1978; Segatz et al., 1988). It will be shown in Section 3 and Appendices E and F that for a wide range of parameters, the primary role of the viscosity is to set the tidal phase lag without altering the amplitude of the response.

2.3. General features of the shallow-water tidally-forced system

In Fig. 1, we show a solution for the spectral coefficients from the semi-analytic method for a model global ocean on Europa (see parameters in Tables 1 and 2) including all tidal components. Even though in this case the eccentricity is ten times larger than the assumed obliquity, the dominant tidal component is the westward obliquity response ($l = 1$), as pointed out in Tyler (2008). The spherical harmonic modes are coupled in degree because of the Coriolis force. This coupling is fairly weak, and the response has power primarily in the modes around the large scale tidal forcing. For the westward propagating obliquity response, the responses at degrees 2 and 3 have much smaller amplitudes than that at degree 1. Degrees 2 and 3 dominate the eccentricity response. For degrees $l > 3$, all responses are negligible. This separation between degrees 3 and 4 allows us to carry out the scaling arguments presented in Section 3.

A key input parameter to the system is the value of the dissipation coefficient, α or ν. We present the average kinetic energy and

Table 1
Constant parameters used in thermal energy calculations.

Parameter	Value	First reference
H	4.5×10^{-12} W kg^{-1}	Section 5.1
ρ_{sil}	3500 kg m^{-3}	Eq. (65)
ρ_{ice}	950 kg m^{-3}	Eq. (65)
Q_{sol}	100	Eq. (66)
G	6.67×10^{-11} m^3 kg^{-3} s^{-2}	Eq. (66)
μ	4×10^9 N m^{-2}	Eq. (67)
c'	0.33	Eq. (68)
ρ (ocean)	1000 kg m^{-3}	Eq. (24)
h	30 km	Eq. (2)
c_D	0.002	Eq. (54)

Table 2
Satellite specific parameters used in thermal energy calculations. The physical parameters on the left half of the table are taken from Schubert et al. (2004) for the Galilean satellites, Thomas (2010), Zebker et al. (2009) and Jacobson et al. (2006) for the saturnian satellites, Thomas (1988) and Jacobson et al. (1992) for the uranian satellites, and Thomas (2000) and Jacobson (2009) for Triton. The orbital parameters are taken from JPL satellite ephemerides (http://ssd.jpl.nasa.gov/?sat_elem). Calculations for the quantities on the right side of the table are described in Section 5.1; measured (as opposed to calculated) quantities are indicated with *. The gravity coefficients for the Galilean satellites are from *Galileo* measurements (Schubert et al., 2004); others are calculated from a hydrostatic assumption. The obliquity for Titan is taken to be the observed value (Stiles et al., 2008) and is not a theoretical Cassini state value.

	R (km)	ρ_{sat} (kg m^{-3})	g (m/s^2)	Ω (rad/s)	p	e	i (deg)	k_2	J_2	$C_{2,2}$	$-\theta_0$ (deg)
Europa	1565.0	2989	1.31	2.05×10^{-5}	-3.10×10^{3}	0.0094	0.466	2.08×10^{-1}	4.36×10^{-4}*	1.32×10^{-4}*	0.053
Ganymede	2631.2	1942	1.43	1.02×10^{-5}	-6.77×10^{3}	0.0013	0.177	2.42×10^{-1}	1.28×10^{-4}*	3.83×10^{-5}*	0.033
Callisto	2410.3	1834	1.24	4.36×10^{-6}	-7.42×10^{3}	0.0074	0.192	1.89×10^{-1}	3.27×10^{-5}*	1.02×10^{-5}*	0.24
Mimas	198.2	1150	0.064	7.72×10^{-5}	-3.82×10^{2}	0.0196	1.574	5.73×10^{-4}	1.43×10^{-2}	4.30×10^{-3}	0.041
Enceladus	252.1	1610	0.11	5.31×10^{-5}	-6.29×10^{2}	0.0044	0.003	1.81×10^{-3}	4.83×10^{-3}	1.45×10^{-3}	0.00014
Tethys	531.0	985	0.15	3.85×10^{-5}	-9.64×10^{2}	0.0001	1.091	3.01×10^{-3}	4.17×10^{-3}	1.25×10^{-3}	0.039
Dione	561.4	1478	0.23	2.66×10^{-5}	-1.56×10^{3}	0.0022	0.028	7.56×10^{-3}	1.32×10^{-3}	3.97×10^{-4}	0.0020
Rhea	763.5	1237	0.26	1.61×10^{-5}	-2.90×10^{3}	0.0002	0.333	9.78×10^{-3}	5.73×10^{-4}	1.74×10^{-4}	0.030
Titan	2574.73	1882	1.35	4.56×10^{-6}	-1.61×10^{4}	0.0288	0.306	2.21×10^{-1}	–	–	0.32*
Miranda	235.8	1200	0.079	5.15×10^{-5}	-4.58×10^{3}	0.0013	4.338	8.84×10^{-4}	6.10×10^{-3}	1.83×10^{-3}	0.021
Ariel	578.9	1665	0.27	2.89×10^{-5}	-8.30×10^{3}	0.0012	0.041	1.02×10^{-2}	1.39×10^{-3}	4.16×10^{-4}	0.00050
Umbriel	584.7	1399	0.23	1.76×10^{-5}	-1.12×10^{4}	0.0039	0.128	7.35×10^{-3}	6.13×10^{-4}	1.84×10^{-4}	0.0026
Titania	788.9	1714	0.38	8.35×10^{-6}	-8.20×10^{3}	0.0011	0.079	1.99×10^{-2}	1.13×10^{-4}	3.38×10^{-5}	0.014
Oberon	761.4	1630	0.35	5.40×10^{-6}	-5.30×10^{3}	0.0014	0.068	1.68×10^{-2}	4.13×10^{-5}	1.48×10^{-5}	0.075
Triton	1353.4	2060	0.78	1.24×10^{-5}	-4.27×10^{4}	0.000	156.87	8.11×10^{-2}	2.07×10^{-4}	6.20×10^{-5}	0.35

energy dissipation for a range of hypothetical viscosities in Figs. 2 and 3. The value of the viscosity is important in this model for two main reasons. First, the value of the viscosity determines the behavior of the response to the westward propagating obliquity tide. For the tidal responses not due to the westward propagating obliquity tide, the behavior is fairly straightforward. The average kinetic energy is relatively independent of the value of the dissipation coefficient prescribed for a large range of values ($\nu \lesssim 10^6$ m^2/s in Fig. 2). For the westward obliquity response, the behavior is different; there is a parameter regime where the amount of kinetic energy, and thus the flow velocities, are sensitive to the prescribed value of ν. Additionally, in this regime, the obliquity response may be less important than the eccentricity response. Second, and of more importance for models of thermal evolution, the energy dissipation rate depends on the viscosity. Thus, determination of a satellite's thermal and orbital history hinges on the prescribed value for the viscosity, which is in reality very poorly constrained. We address this issue in Section 4.

3. Scaling laws for tidally-driven ocean flows

The shallow-water system presented in Section 2 can be solved using a semi-analytic method with computational ease. The challenge in understanding the ocean response to the tidal forcing is determining how the various input parameters affect the resulting

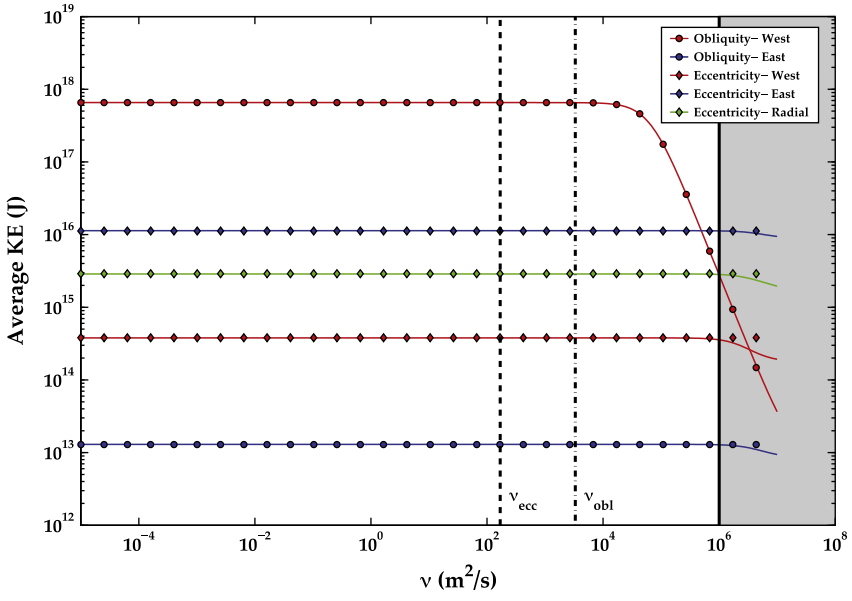

Fig. 2. Average kinetic energy associated with each of the tidal responses for an ocean on Europa with parameters from (Tables 1 and 2), where symbols indicate the values calculated from scaling arguments (Section 3 and Appendices E and F) and the solid lines indicate values calculated through the semi-analytic solution (Section 2.2). The shaded region indicates where the Reynolds number is less than 50 for this model ocean and the scaling argument predictions are no longer within 10% of the semi-analytic solution value (see (29)). The dashed line represents the effective viscosity for the response to the eccentricity tide and the dot-dashed line represents that for the obliquity tide, both of which are numerically-derived (see Section 4.2) using the same coefficient of drag ($c_D = 0.002$). Note that these effective viscosities are not the same, making the obliquity tide the likely dominant contributor to the ocean energy dissipation (see Section 5.2 for further details).

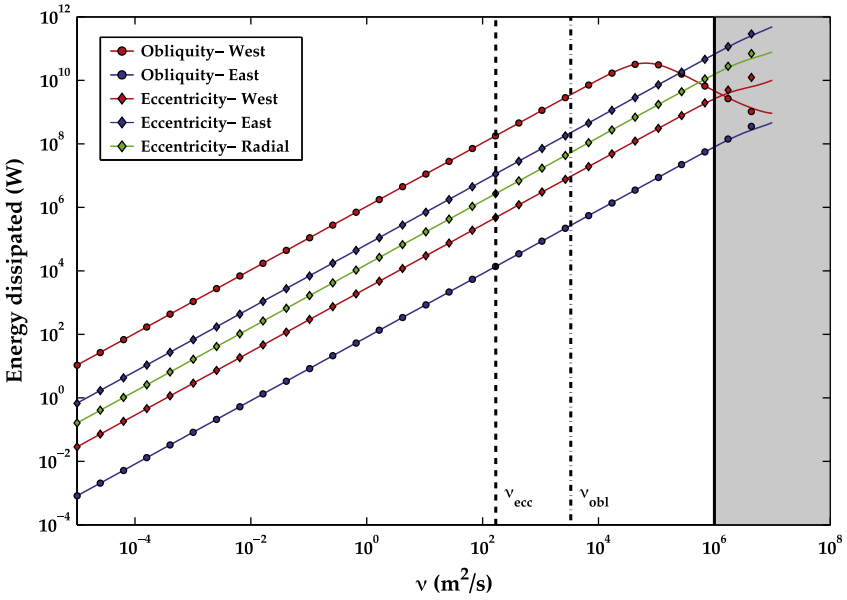

Fig. 3. Similar to Fig. 2 but for average energy dissipation.

flow and choosing an appropriate value for ν or α. We address the first issue here and discuss an estimate for the effective ocean viscosity in Section 4.

The shallow water system presented in Section 2.2 involves series solutions that are coupled in spherical harmonic degree. However, as can be seen in Fig. 1, the power decreases quite rapidly with increasing spherical harmonic degree l. The tidal responses, previously represented as infinite sums or for numeric purposes as a truncated series, can be reasonably estimated by using a very limited number of modes (typically 2–3) without any significant loss of accuracy. Instead of solving the system of equations given by (21) and (22) numerically, we now solve the system algebraically.

The benefits of these solutions are multifold. First, the simplifications we present make the underlying physics more transparent than the fully coupled problem. Second, these solutions provide relations for the kinetic energy and energy dissipation in terms of the various input parameters (e.g. R, g, h, Ω), instead of the spherical harmonic coefficients. These relations provide insight into the sensitivity of the solutions to the various input parameters that themselves may have a degree of uncertainty. Additionally, these relations are simple to implement in orbital evolution models and are likely accurate in most scenarios, similar to the familiar solid-body tidal heating equations (Segatz et al., 1988; Wisdom, 2008). These scalings are limited in that they do not address the issue that the ocean's effective viscosity is essentially unconstrained, but we will use these scalings to inform the estimates of the viscosity that we present in Section 4.

In addition to the tidal forcing, the ocean responds to three forces (cf. momentum Eq. (1)): pressure gradients in the form of surface gravity waves, the Coriolis force, and the drag. For the scalings we suggest below, we need the ratios of these forces. We adopt a Navier–Stokes viscosity such that the role of viscosity can be compared to that of rotation through a rotational Reynolds number Re,

$$Re \equiv \frac{\Omega R^2}{\nu},$$

where the characteristic velocity is taken to be the linear rotational speed, not the typical ocean flow velocity, and the characteristic length scale is R. We are also concerned with the square of the ratio of the linear rotational speed to the surface gravity wave speed, ϵ, called the Lamb parameter in Longuet-Higgins (1968),

$$\epsilon \equiv \frac{4\Omega^2 R^2}{gh}.$$

Below, we present scaling arguments which allow us to analytically calculate the ocean response, the average kinetic energy and average energy dissipation rate in the case of Navier–Stokes type dissipation. The algebra in the following section can be tedious; we present scalings for the response to the westward propagating obliquity tidal potential here and direct the reader to Appendices E and F for details associated with the other components of the tide. For those uninterested in the details, we summarize all of the scaling results in Table 4. These estimates are accurate to 10% of the full solutions from Section 2.2 if the following limits are satisfied, high Reynolds number,

$$Re \geq 50, \tag{29}$$

and small Lamb parameter,

$$\epsilon \leqslant \frac{4}{15}. \tag{30}$$

For typical satellite oceans, where the rotation rate and satellite radius are well-known, these limits should be thought of as low effective viscosity ($\nu \lesssim 10^6$ m^2/s) and thick oceans ($h \gtrsim 10$ km), respectively. Because the molecular viscosity of water is very small, the scaling constraint (29) should be appropriate for all satellite oceans. Earth lies in a high Lamb parameter regime because the oceans on Earth are far shallower than those presumed to exist on the icy satellites (Khurana et al., 1998). In the small Lamb parameter regime, the time lag between the forcing potential and the ocean's response is small because the gravity wave speed is fast in comparison to the surface rotational speed; as the tidal potential changes, the gravity waves can rapidly propagate this disturbance.

Under these limits, we now present the analysis for the response to the westward propagating obliquity tide. This is likely to be the dominant ocean response for many satellite parameters (as recognized in Tyler (2008)) but for completeness, we also direct the reader to Appendices E and F for details related to the other tidal components. As discussed below, the obliquity tide involves a resonant response which can drive large flows. Other resonant

modes exist, but typically require very thin oceans (Tyler, 2011). We therefore ignore these modes, because of the expected thicknesses (tens of km) of most icy satellite oceans (see Section 5.5).

3.1. Scalings for the response to the westward obliquity tidal potential

Looking at the response to the westward obliquity tide (Fig. 1), the dominant component of the power spectrum is the $l = 1$ term (i.e. Ψ_1^1). This response is coupled through the Coriolis force to Φ_2^1 and the forcing tide. We thus carry out this scaling analysis with the assumption that the response is accurately captured by only the $l = 1$ and $l = 2$ terms. The vorticity Eq. (21) for Ψ_1^1 here written in terms of the Reynolds number and Lamb parameter is

$$\left[i + \frac{2}{Re} - i\frac{2(1)}{(1)(2)}\right]\Psi_1^1 - 2\left[\frac{3}{2}C_2^1\Phi_2^1\right] = 0. \tag{31}$$

The first imaginary term in (31) represents the ocean response while the second imaginary term represents a Rossby–Haurwitz wave. In this instance, these two exactly cancel, and we obtain

$$\Psi_1^1 = \frac{3C_2^1}{2}Re\Phi_2^1, \tag{32}$$

where the amplitude of the response grows as the viscosity decreases, and Reynolds number increases; this is the resonance that Tyler (2008) refers to. For other tidal responses (see Appendices E and F), the imaginary terms do not disappear and in fact, are much larger than the Reynolds number term. These terms limit the response amplitude and, therefore, the overall behavior of the other responses differ dramatically from that of the westward obliquity response.

The amplitude of Ψ_1^1 is related to Φ_2^1 by the horizontal divergence Eq. (22)

$$\left[i\frac{2}{3} + \frac{6}{Re} - i\frac{24}{\epsilon}\right]\Phi_2^1 + \frac{3}{2}\left(C_2^1\right)^2 Re\Phi_2^1 \approx \frac{-U_2^1}{\Omega} \tag{33}$$

when the relation (32) is substituted and the contribution from Ψ_3^1 is neglected. In the appropriate scaling limits (large Reynolds number and small Lamb parameter), the dominant terms of (33) are

$$\left(\frac{3}{2}\left(C_2^1\right)^2 Re - i\frac{24}{\epsilon}\right)\Phi_2^1 \approx \frac{-U_{2,W}^1}{\Omega}. \tag{34}$$

The total kinetic energy (24) of the response is dominated by Ψ_1^1 (Fig. 1) and can be approximated as

$$E_{tot} \approx 2\rho h\left|\Psi_1^1\right|^2 = \frac{9\left(C_2^1\right)^2}{2}\rho h Re^2\left|\Phi_2^1\right|^2, \tag{35}$$

when the relation (32) is included. Recasting (34), we have

$$\begin{aligned}\left|\Phi_2^1\right|^2 &\approx \frac{\left|U_{2,W}^1\right|^2}{\Omega^2\left|\frac{3}{2}\left(C_2^1\right)^2 Re - i\frac{24}{\epsilon}\right|^2} \\ &= \frac{4\left|U_{2,W}^1\right|^2}{\Omega^2 Re^2\left(9\left(C_2^1\right)^4 + 2304\left(\frac{1}{\epsilon Re}\right)^2\right)}.\end{aligned} \tag{36}$$

Substituting (6) and (36) into (35), the kinetic energy of the response is given as

$$\begin{aligned}E_{tot} &\approx \frac{18\left(C_2^1\right)^2\rho h\left|U_{2,W}^1\right|^2}{\Omega^2\left(9\left(C_2^1\right)^4 + 2304\left(\frac{1}{\epsilon Re}\right)^2\right)} \\ &= \frac{27\left(C_2^1\right)^2\pi}{5}\frac{\rho h\Omega^8 R^{12}\theta_0^2}{\left(9\left(C_2^1\right)^4\Omega^6 R^8 + 144\nu^2 g^2 h^2\right)}.\end{aligned} \tag{37}$$

In similar fashion, the average energy dissipation (27) can be approximated as

$$\dot{E} \approx \frac{2\rho h\nu}{R^2}(1)^2(2)^2\left|\Psi_1^1\right|^2 = 18\left(C_2^1\right)^2\rho h\Omega Re\left|\Phi_2^1\right|^2. \tag{38}$$

Substituting (6) and (36) into (38), the energy dissipated by the response is given as

$$\begin{aligned}\dot{E} &\approx \frac{72\left(C_2^1\right)^2\rho h\left|U_{2,W}^1\right|^2}{\Omega Re\left(9\left(C_2^1\right)^4 + 2304\left(\frac{1}{\epsilon Re}\right)^2\right)} \\ &= \frac{108\left(C_2^1\right)^2\pi}{5}\frac{\rho h\nu\Omega^8 R^{10}\theta_0^2}{\left(9\left(C_2^1\right)^4\Omega^6 R^8 + 144\nu^2 g^2 h^2\right)}.\end{aligned} \tag{39}$$

We may also use Eq. (37) to derive an average flow speed $\bar{u}$:

$$\begin{aligned}\bar{u} &= \frac{3\left(C_2^1\right)\left|U_{2,W}^1\right|}{\sqrt{\pi}\Omega R\left(9\left(C_2^1\right)^4 + 2304\left(\frac{1}{\epsilon Re}\right)^2\right)^{1/2}} \\ &= \sqrt{\frac{27}{50}}\frac{\Omega^4 R^5\theta_0}{\left(9\left(C_2^1\right)^4\Omega^6 R^8 + 144\nu^2 g^2 h^2\right)^{1/2}}.\end{aligned} \tag{40}$$

The scalings (37), (39) and (40) are the general form for high Reynolds number and small Lamb parameter as defined in (29) and (30). While the scalings are cumbersome, these values are simple to calculate in a numerical code. As mentioned previously, it is clear from Figs. 2 and 3 that the response to the westward propagating obliquity tide can be split into two behavioral regimes; which regime applies depends on the product of the Reynolds number and the Lamb parameter, $\frac{1}{\epsilon Re}$. We present further simplifications for these two regimes in order to highlight the underlying force balances and behavioral physics.

For high Reynolds numbers ($\frac{1}{\epsilon Re} \lesssim \frac{1}{80}$), the Rossby–Haurwitz wave response dominates the bulk behavior. Ignoring the gravity wave contribution in (34), Φ_2^1 is

$$\Phi_2^1 \approx \frac{-U_{2,W}^1}{\Omega\left(\frac{3}{2}\left(C_2^1\right)^2 Re\right)} = -5\sqrt{\frac{2\pi}{15}}\nu\theta_0, \tag{41}$$

which in turn yields

$$\Psi_1^1 \approx \frac{-U_{2,W}^1}{\left(C_2^1\right)\Omega} = \frac{-3}{2}\sqrt{\frac{2\pi}{3}}\Omega R^2\theta_0. \tag{42}$$

This solution asymptotes to the inviscid solution presented in Tyler (2008). In this regime, the kinetic energy is independent of viscosity,

$$E_{tot} \approx 2\rho h\left|\Psi_1^1\right|^2 = 3\pi\rho h\Omega^2 R^4\theta_0^2, \tag{43}$$

and we can derive an average flow speed $\bar{u}$ of

$$\bar{u} = \left(\frac{3}{2}\right)^{1/2}\Omega R\theta_0. \tag{44}$$

This makes intuitive sense: if viscosity is not impeding flow significantly, the flow speed is controlled by the rate at which the tidal bulge is moving around the body. From (27) or (28), the associated energy dissipation scaling scales linearly with the viscosity

$$\dot{E} \approx 12\pi\rho h\nu\Omega^2 R^2\theta_0^2 = 8\rho h\nu\bar{u}^2. \tag{45}$$

For lower Reynolds numbers ($\frac{1}{\epsilon Re} \gtrsim \frac{1}{80}$), while still remaining in the scaling limits defined by (29) and (30), the gravity waves dominate the response. Then,

$$\Phi_2^1 \approx \frac{U_{2,W}^1}{\Omega\left(\frac{i24}{\epsilon}\right)} = \frac{-i}{4}\sqrt{\frac{2\pi}{15}}\frac{\Omega^3 R^4 \theta_0}{gh} \tag{46}$$

and therefore

$$\Psi_1^1 \approx \frac{3}{2}\frac{C_2^1 U_{2,W}^1 Re}{\Omega\left(\frac{i24}{\epsilon}\right)} = \frac{-i3}{40}\sqrt{\frac{2\pi}{3}}\frac{\Omega^4 R^6 \theta_0}{vgh}. \tag{47}$$

In this regime, the viscosity has altered the natural frequency of the system, and thus the response amplitudes no longer behave resonantly. The kinetic energy now depends on the value of the Reynolds number,

$$E_{tot} \approx 2\rho h\left|\Psi_1^1\right|^2 \approx \frac{\left(C_2^1\right)^2\pi}{320}\rho h\Omega^2 R^4\theta_0^2(\epsilon Re)^2 = \frac{3\pi}{400}\frac{\rho\Omega^8 R^{12}\theta_0^2}{v^2 g^2 h} \tag{48}$$

with an associated average flow speed of

$$\bar{u} = \left(\frac{3}{800}\right)^{1/2}\frac{\Omega^4 R^5\theta_0}{vgh}. \tag{49}$$

In this limit flow speeds decrease as viscosity increases. The associated energy dissipation is now inversely proportional to the viscosity,

$$\dot{E} \approx \frac{3\pi}{100}\frac{\rho\Omega^8 R^{10}\theta_0^2}{vg^2 h}. \tag{50}$$

The shape of the energy dissipation curve (Fig. 3) can be thought of as the product of two effects: the bulk flow velocity and the value of the viscosity. This peak in dissipation rate is similar to that seen for Maxwell viscoelastic dissipation in solid bodies (Ross and Schubert, 1989). For the high Reynolds number regime, the velocities are high but the viscosity is too low to generate significant dissipation. In the lower Reynolds number regime, the viscosity is large and thus can dissipate energy. But in analogy with forced-damped harmonic oscillators, the viscosity has moved the natural frequency of the system sufficiently away from the forcing frequency that the response no longer has large resonant amplitudes.

3.2. Effective tidal quality factor Q in a satellite ocean

Throughout this section, we have considered viscous effects through a Navier–Stokes viscosity, primarily because this allows for parameterization in the form of the Reynolds number. These scalings can also be expressed in terms of an effective tidal quality factor Q, which can in turn be related to the linear drag coefficient α mentioned in Section 2. Q is defined as (Murray and Dermott, 1999),

$$Q \equiv \frac{2\pi E_{tot}}{\dot{E}\left(\frac{2\pi}{\Omega}\right)} = \frac{\Omega E_{tot}}{\dot{E}} \tag{51}$$

and is related to the linear drag coefficient α by (Tyler, 2011),

$$\alpha = \frac{\Omega}{2Q}. \tag{52}$$

For the westward propagating obliquity tide, by substituting (43), (45), (48) and (50), we find that the tidal quality factor is simply

$$Q_{obl,W} \approx \frac{1}{4}\left(\frac{\Omega R^2}{\nu}\right) = \frac{1}{4}Re \tag{53}$$

for all regimes. We emphasize that this is an effective Q, in attempting to maintain consistency with the terminology used in Tyler (2011). This Q is different from that typically defined for solid-body tidal heating (Peale et al., 1979; Murray and Dermott, 1999) in that the dissipation is referenced to the kinetic energy of the ocean, instead of the stored elastic energy due to the tide.

The effective Q of the Earth is known ($Q = 12$; Murray and Dermott (1999)) from lunar laser ranging, and is due mainly to ocean dissipation. Unfortunately, the Earth's ocean is in many ways quite different to that on an icy satellite: it spins non-synchronously, it has bottom topography that is comparable to the ocean thickness, and it is stably stratified in some regions (see Section 5.5). As a result, it is hard to use this particular observational constraint to derive an effective Q for icy satellites. Instead we adopt an approach based on an empirically-derived friction coefficient, as described next.

4. Effective viscosity in a global ocean

The scalings presented in Section 3 provide a description of global ocean behavior; however, to estimate the energy dissipation in the ocean, these scalings require a prescribed value for the effective viscosity. This viscosity is unlikely to be as small as the molecular viscosity, presumably due to turbulence (Pope, 2000), but it is unclear how large an effective viscosity one should adopt (Lumb and Aldridge, 1991). While there is potential to infer from measurements what the effective viscosity is for a global liquid layer, such as for the liquid core of Earth (Smylie, 1999; Mound and Buffett, 2007; Buffett and Christensen, 2007) or Mercury, it is unlikely that we can do so for icy satellite oceans. Also, while these measurements can give some insight into the effects of turbulence, the effective viscosity is likely to be time-variable, changing with flow conditions and/or degree of turbulence (Brito et al., 2004).

Because of the high degree of variability amongst satellites of the outer Solar System both in the past and at present, it is unlikely that a single value for the effective ocean viscosity can be broadly applied. Thus, we approach the question of what the effective viscosity in a satellite ocean is by analogy with the Earth's oceans. On Earth, there is a long history of estimating dissipation of tides due to bottom boundary friction (Taylor, 1920; Jeffreys, 1921; Munk and MacDonald, 1960). While the drag coefficient c_D (see Eq. (54) below) was originally empirically-based (Taylor, 1920), a value c_D of O (0.001) is still commonly used, even in more modern numerical ocean models (Jayne and Laurent, 2001; Egbert and Ray, 2001). Sohl et al. (1995) discuss what value of c_D to apply to Titan's ocean. Taking the weak dependence of c_D on Reynolds number into account, these authors conclude that values in the range 0.002–0.01 are likely appropriate for liquid water.

We incorporate a c_D-based parameterization into the shallow water model for a global ocean. This approach is undeniably simplistic. However, when given the alternative of choosing a value for the effective viscosity where the uncertainty is approximately twelve orders of magnitude (Lumb and Aldridge, 1991), we favor our approach, although there are caveats. We address these in Section 5.5. While we adopt the value $c_D = 0.002$ in this work, the results and scalings that we present in Section 4.2 are general (and linear) for c_D, and thus, permit the effect of uncertainties in c_D to be readily explored.

4.1. Numerical method

The momentum equation for an ocean subject to tidal forcing and bottom boundary friction is (cf. (Jayne and Laurent, 2001))

$$\frac{\partial\vec{u}}{\partial t} + 2\vec{\Omega}\times\vec{u} = -g\vec{\nabla}\eta - \vec{\nabla}U - \frac{c_D}{h}|\vec{u}|\vec{u}. \tag{54}$$

Similar to the process in Section 2.2, we can employ a Helmholtz decomposition and write the divergence and the radial component of the curl of (54) as

$$\left[\left(\frac{\partial}{\partial t}\right)\nabla^2 + \frac{2\Omega}{R^2}\frac{\partial}{\partial\phi}\right]\Phi + 2\Omega\left[\cos\theta\nabla^2 - \frac{\sin\theta}{R^2}\frac{\partial}{\partial\theta}\right]\Psi = -g\nabla^2\eta - \nabla^2 U - \left(\frac{c_D}{h}\vec{\nabla}\cdot(|\vec{u}|\vec{u})\right), \tag{55}$$

$$\left[\left(\frac{\partial}{\partial t}\right)\nabla^2+\frac{2\Omega}{R^2}\frac{\partial}{\partial\phi}\right]\Psi-2\Omega\left[\cos\theta\nabla^2-\frac{\sin\theta}{R^2}\frac{\partial}{\partial\theta}\right]\Phi = -\left(\frac{c_D}{h}\hat{r}\cdot(\vec{\nabla}\times(|\vec{u}|\vec{u}))\right). \quad (56)$$

While the solutions to (55) and (56) are likely oscillatory, the nonlinearity of the dissipative term requires that we integrate the system numerically. We seek solutions of the form

$$\Psi(\theta,\phi,t)=\sum_{l=1}^{NL}\sum_{m=1}^{l}\left[\Psi_l^m Y_l^m+\Psi_l^{-m}Y_l^{-m}\right] = 2\Re\left(\sum_{l=1}^{NL}\sum_{m=1}^{l}\left[\Psi_l^m Y_l^m\right]\right), \quad (57)$$

and similarly for Φ and η. Here the coefficients Ψ_l^m (and their equivalents Φ_l^m, and η_l^m) are still complex but are now functions of time, and NL is the series truncation level. Plugging in (57) and its equivalents into (55), (56) and (18), and projecting the resulting equations onto individual spherical harmonics, the system of equations to solve is

$$\left[\frac{\partial}{\partial t}-\frac{2\Omega i m}{l(l+1)}\right]\Psi_l^m-2\Omega\left[\frac{l-1}{l}C_l^m\Phi_{l-1}^m+\frac{l+2}{l+1}C_{l+1}^m\Phi_{l+1}^m\right] = \frac{R^2}{l(l+1)}\left(\frac{c_D}{h}\hat{r}\cdot(\vec{\nabla}\times(|\vec{u}|\vec{u}))\right)_l^m \quad (58)$$

$$\left[\frac{\partial}{\partial t}-\frac{2\Omega i m}{l(l+1)}\right]\Phi_l^m+2\Omega\left[\frac{l-1}{l}C_l^m\Psi_{l-1}^m+\frac{l+2}{l+1}C_{l+1}^m\Psi_{l+1}^m\right] = -g\eta_l^m+\frac{R^2}{l(l+1)}\left(\frac{c_D}{h}\vec{\nabla}\cdot(|\vec{u}|\vec{u})\right)_l^m-2U_2^0\cos(\Omega t)\delta_{l,2}\delta_{m,0} - 2U_{2,W}^1\cos(\Omega t)\delta_{l,2}\delta_{m,1} - \left[\left(U_{2,W}^2+U_{2,E}^2\right)\cos(\Omega t)+\left(U_{2,W}^2-U_{2,E}^2\right)i\sin(\Omega t)\right]\delta_{l,2}\delta_{m,2}, \quad (59)$$

$$\frac{\partial\eta_l^m}{\partial t}-\frac{hl(l+1)}{R^2}\Phi_l^m=0. \quad (60)$$

These equations are coupled in both spherical harmonic degree l and order m through the dissipative terms on the right hand side of Eqs. (58) and (59). We include all components of the tide in (59) because nonlinearity has the ability to couple different spherical harmonic orders, while previously these were separable. Because we have not assumed wave solutions, we now have to solve explicitly for the spherical coefficients of η, whereas we previously assumed the relationship (20) between η and Ψ.

Eqs. (58)–(60) are nonlinear and thus cannot be solved with the semi-analytic method previously employed in Section 2.2. Instead of assuming wave solutions as in Section 2.2, we employ a numerical integration method where the time derivatives are explicitly treated using the Adams–Bashforth method. We calculate the nonlinear dissipative terms using a spectral-transform method. The horizontal velocities are calculated on a spherical grid which consists of 100 evenly spaced grid points in longitude and 50 Gauss–Lobatto nodes in colatitude. The frictional dissipation contributions are calculated on this grid, and subsequently, transformed back into their spherical harmonic decomposition. To reduce the required number of spectral coefficients, we added an enhanced Navier–Stokes dissipative term of the form $\nu l(l+1)/R^2$ with $\nu=1\times10^8$ m^2/s to (58) and (59) for all coefficients with l = NL (the series truncation level) and l = NL − 1. We adopt a series truncation level of NL = 30. The enhanced dissipative terms reduce the required truncation level by an order of magnitude without affecting the results presented here; for example, the amount of energy dissipated for our model Europan ocean is approximately 10^9 W total, and the amount dissipated from the enhanced dissipation term is less than 0.1 W.

We have run a series of numerical integrations varying the seven input parameters (i.e. $R, g, h, \Omega, \theta_0, e$, and c_D) to understand the sensitivity of the system to each. These numerical integrations are initialized to either zero or the semi-analytic solution; the steady-state solution is independent of these values. We evolve the equations in time until they produce a constant solution for the kinetic energy and energy dissipation when averaged over an orbital period, similar to the behavior of the linear solution (cf. (24) and (27)).

4.2. Scaling arguments

The shallow water system including nonlinear bottom drag settles on a wave solution. While the dissipation processes are not exactly alike, we can assume that the previous linear Navier–Stokes formulation is equivalent, in a time-averaged sense, to the nonlinear bottom drag with

$$-\frac{c_D}{h}|\vec{u}|\vec{u}\sim\nu\nabla^2\vec{u}. \quad (61)$$

which implies that

$$\nu\sim\frac{c_D R^2|\vec{u}|}{l(l+1)h}, \quad (62)$$

where the lengthscale associated with the Laplacian is taken to be $R/\sqrt{l(l+1)}$. Assuming that $|\vec{u}|$ scales with the average velocity, we find the scalings

$$\nu_{eff,obl}=k_{obl}\frac{c_D}{h}\frac{\Omega^4R^7\theta_0}{\left(9(C_2^1)^4\Omega^6R^8+144\nu_{eff,obl}^2g^2h^2\right)^{1/2}} \quad (63)$$

by using the relation (40) for the obliquity-related response and

$$\nu_{eff,ecc}=k_{ecc}\frac{c_D\Omega^3R^5e}{gh^2} \quad (64)$$

by using (F.10), (F.20) and (F.29) for the eccentricity response. From our numerical runs, the least squares fit for k_{obl} is 0.40 and k_{ecc} is 0.13.

The value of the scaling parameters in Eqs. (63) and (64) may be approximated analytically by taking the flow speeds from Table 4 and substituting into Eq. (62). For the eccentricity tide, this yields $k_{ecc}\approx\sqrt{57/112}/l(l+1)\approx0.12$, taking $l=2$. For the obliquity tide, we obtain $k_{obl}\approx\sqrt{27/50}/l(l+1)\approx0.37$, taking $l=1$. These analytical approximations agree very well with the numerical results.

The effective viscosity for obliquity (63) can be solved quadratically (see Table 4), and displays simpler behavior in the low and high Reynolds number limits discussed in Section 3.1. For a model ocean on Europa, the numerically-derived effective viscosity is $\nu_{eff,obl}=3.3\times10^3$ m^2/s for the obliquity-related flow and $\nu_{eff,ecc}=1.7\times10^2$ m^2/s for the eccentricity-related flow.

4.3. Summary

The numerically derived scalings (63) and (64) provide estimates for the effective viscosity given a set of input parameters. These viscosities can be input into either the semi-analytic system (Section 2.2) or the scaling laws (see Table 4) in order to determine the flow response and energy dissipation rate of a satellite ocean. It is worth noting that the effective viscosities for the obliquity and eccentricity responses scale differently with the input parameters because the velocities scale differently between the two responses. These values for a model Europan ocean are displayed in Figs. 2 and

3 for reference. In the context of thermal–orbital evolution models, where the input parameters change over time, the scalings for the viscosities are critical to better estimating the long-term impact of ocean tidal heating.

5. Implications for the outer Solar System satellites

With estimates of effective viscosity in hand, it is now possible to complete a survey of the thermal heat budgets for various satellites of the outer Solar System. Specifically, we seek to answer two fairly broad questions: should ocean tidal heating be an important heat source at present for any of the icy satellites; and could ocean tidal heating have been a significant heat source in the past? These questions are difficult to answer in that there are many uncertainties in the parameters that go into the following calculations. Because our goal was to understand broad trends and not to explain specific observations or quantities, we have used simplified theoretical models in order to calculate the thermal budgets, with the understanding that these results may diverge from what is observed, as for example in the long-recognized anomalous cases of Mimas or Enceladus (Squyres et al., 1983; Meyer and Wisdom, 2007; Howett et al., 2011).

5.1. Calculating the available thermal energy

The primary heat sources available to a satellite are radiogenic heat and tidal dissipation, either in the solid ice and rock layers or in a liquid ocean layer. For the radiogenic component of the thermal budget, we assume a chondritic heating rate of $H = 4.5 \times 10^{-12}$ W kg^{-1} (Ellsworth and Schubert, 1983). We calculate an equivalent silicate mass, M_{sil}, assuming a two-component satellite

$$M_{sil} = \frac{4}{3}\rho_{sil}\left(\frac{\rho_{sat}-\rho_{ice}}{\rho_{sil}-\rho_{ice}}\right)\pi R^3 \tag{65}$$

where the silicate density is taken as $\rho_{sil} = 3500$ kg m^{-3}, the ice density is taken as $\rho_{ice} = 950$ kg m^{-3}, and the satellite mean density ρ_{sat} as presented for various satellites in Table 2.

To estimate the amount of solid body tidal heating, we employ the standard viscoelastic model (Segatz et al., 1988; Ross and Schubert, 1989; Wisdom, 2004). In this model, the rate of solid body dissipation is given by

$$\dot{E} = \frac{3}{2}\frac{k_2}{Q_{sol}}\frac{(\Omega R)^5}{G}(7e^2 + \sin^2\theta_0), \tag{66}$$

where the satellite structure and dissipation characteristics are parameterized by the tidal Love number, k_2, and the tidal quality factor, Q_{sol}, and G is the gravitational constant. For the unknown satellite parameters, k_2 and Q_{sol}, we adopt a value of Q_{sol} of 100 (Goldreich and Soter, 1966), and we estimate the Love number using Kelvin's formula (Love, 1944),

$$k_2 = \frac{3/2}{1+\frac{19\mu}{2\rho_{sat}gR}} \tag{67}$$

for a homogeneous body with rigidity, μ, assumed to be $\mu = 4.0 \times 10^9$ N m^{-2}. We also calculate the dissipation with a homogeneous fluid k_2 of 3/2 to understand the energy budget in the limit of a fully deformable body, such as one with an ocean.

In previous works, the dissipation related to the obliquity tide has typically been neglected, primarily because it is assumed that the obliquity is small and also, until recently, there have been no measurements of satellite obliquity. While for most satellites the obliquity solid body tidal dissipation is negligible when compared to the eccentricity driven solid body dissipation, this relationship is reversed in the case of ocean tidal heating.

Titan is currently the only icy satellite with a measured obliquity (Stiles et al., 2008). In order to estimate the contributions to other satellites from the obliquity tide, we have assumed obliquities appropriate for satellites in damped Cassini states with a single orbit precession frequency; interactions with other satellites do not generally change the results significantly (Bills, 2005; Baland et al., 2012). In a Cassini state, the invariable pole, orbit normal, and spin pole remain coplanar as they precess (Colombo, 1966; Peale, 1969). For this coplanar precession to occur, the obliquity must satisfy the relation (Peale, 1969; Ward, 1975; Bills and Nimmo, 2008)

$$\frac{3}{2}[(J_2 + C_{2,2})\cos\theta_0 + C_{2,2}]p\sin\theta_0 = c'\sin(i-\theta_0) \tag{68}$$

where J_2 and $C_{2,2}$ are the degree-2 gravity coefficients, i is the orbital inclination, and p is the ratio of the orbital motion to the orbit plane precession and is given by

$$p = \frac{\Omega}{d\Omega_{orb}/dt} \tag{69}$$

where Ω_{orb} is the longitude of the ascending node. The quantity c' is the normalized polar moment of inertia, with the prime denoting the fact that the relevant moment of inertia may be that of a decoupled shell rather than the entire body. We introduce this distinction because of the case of Titan, where the moment of inertia c estimated from gravity measurements (see below) does not equal that inferred from Titan's obliquity (Bills and Nimmo, 2011).

While the orbital parameters are well-established, observations of the gravity coefficients and moment of inertia for many satellites are limited. We estimate the unmeasured gravity coefficients assuming a hydrostatic satellite using the Darwin–Radau relation (Darwin, 1899; Radau, 1885; Hubbard and Anderson, 1978)

$$C_{2,2} = \frac{1}{4}\left(\frac{\Omega^2}{G(\frac{4}{3}\pi\rho_{sat})}\right)\left(\frac{5}{1+\left(\frac{5}{2}-\frac{15}{4}c\right)^2}-1\right) \tag{70}$$

where c denotes the normalized polar moment of inertia of the entire body. For a hydrostatic body $J_2 = 10C_{2,2}/3$.

For the ocean contributions to tidal heating, we estimate the effective viscosities from (63) and (64) for the obliquity and eccentricity tides separately. We use values of h = 30 km and $c_D = 0.002$ for all satellites. After calculating a satellite-specific effective viscosity, the associated tidal dissipation is calculated from the analytical scalings summarized in Table 4; the semi-analytic approach from Section 2.2 produces nearly identical results.

Table 1 summarizes all of the common parameters used in this analysis, while Table 2 shows the parameters used and calculated quantities that are satellite specific. In preparing this Table, we took $c = c' = 0.33$, representative of a differentiated body with no shell decoupling. Increasing c' to 0.67 (a decoupled shell) while keeping $c = 0.33$ results in an increase in the predicted obliquity θ_0 by a factor of roughly 2, and the obliquity-related heating by a factor of roughly 4.

The various contributions to the thermal energy budget are presented for each satellite in Table 3. In Figs. 4–6 we highlight key results that are tabulated in Table 3. In Fig. 4, we present the relative contributions to the ocean tidal dissipation from the eccentricity and obliquity tides. While the obliquity tidal response likely dominates ocean dissipation, there are examples of satellites where the eccentricity response could be more important. The full thermal budgets of many satellites are presented in Figs. 5 and 6 where the solid-body tidal dissipation is calculated using illustrative values of $Q_{sol} = 100$ and k_2 corresponding to an elastic homogenous body or a fully fluid body, respectively. The actual values for these are likely to depend on the details of internal structure and rheology (Ross and Schubert, 1989), and in particular whether a

Table 3
Energy contributions calculated from parameters presented in Tables 1 and 2 as described in Section 5.1. Entries marked [] in final column have $\epsilon > 4/15$ for the nominal parameters.

		Homogeneous k_2		$k_2 = 3/2$			
	$\dot{E}_{rad}(W)$	$\dot{E}_{solid,ecc}(W)$	$\dot{E}_{solid,obl}(W)$	$\dot{E}_{solid,ecc}(W)$	$\dot{E}_{solid,obl}(W)$	$\dot{E}_{ocean,ecc}(W)$	$\dot{E}_{ocean,obl}(W)$
Europa	2.02×10^{11}	9.77×10^{11}	1.34×10^{9}	7.05×10^{12}	9.70×10^{9}	1.47×10^{7}	3.1×10^{9}
Ganymede	4.67×10^{11}	8.79×10^{9}	2.49×10^{8}	5.46×10^{10}	1.55×10^{9}	1.66×10^{4}	1.3×10^{9}
Callisto	3.20×10^{11}	2.08×10^{9}	9.30×10^{7}	1.65×10^{10}	7.40×10^{8}	8.80×10^{2}	3.8×10^{9}
Mimas	4.02×10^{7}	2.90×10^{8}	5.46×10^{4}	7.59×10^{11}	1.40×10^{8}	2.38×10^{7}	$[2.5 \times 10^{6}]$
Enceladus	2.73×10^{8}	2.37×10^{7}	1.04×10^{0}	1.96×10^{10}	8.64×10^{2}	2.32×10^{4}	1.2×10^{-1}
Tethys	1.34×10^{8}	1.70×10^{5}	1.11×10^{6}	8.45×10^{7}	5.51×10^{8}	2.57×10^{1}	$[3.7 \times 10^{7}]$
Dione	2.42×10^{9}	4.25×10^{7}	1.52×10^{3}	8.44×10^{9}	3.02×10^{5}	4.46×10^{3}	2.2×10^{3}
Rhea	3.31×10^{9}	1.73×10^{5}	1.79×10^{5}	2.65×10^{7}	2.75×10^{7}	7.35×10^{-1}	7.5×10^{6}
Titan	4.11×10^{11}	6.43×10^{10}	3.46×10^{8}	4.37×10^{11}	2.35×10^{9}	1.23×10^{5}	1.1×10^{10}
Miranda	8.50×10^{7}	6.17×10^{5}	7.10×10^{3}	1.05×10^{9}	1.21×10^{7}	6.37×10^{2}	2.6×10^{5}
Ariel	3.59×10^{9}	3.00×10^{7}	2.31×10^{2}	4.42×10^{9}	3.40×10^{4}	1.36×10^{3}	5.1×10^{1}
Umbriel	2.32×10^{9}	2.00×10^{7}	4.07×10^{3}	4.08×10^{9}	8.29×10^{4}	9.69×10^{2}	1.8×10^{3}
Titania	9.71×10^{9}	4.71×10^{5}	3.27×10^{3}	3.55×10^{7}	2.46×10^{5}	1.63×10^{-1}	1.3×10^{5}
Oberon	7.76×10^{9}	6.10×10^{4}	7.81×10^{3}	5.44×10^{6}	6.98×10^{5}	5.82×10^{-3}	3.3×10^{6}
Triton	7.12×10^{10}	0	8.70×10^{8}	0	1.60×10^{10}	0	6.6×10^{10}

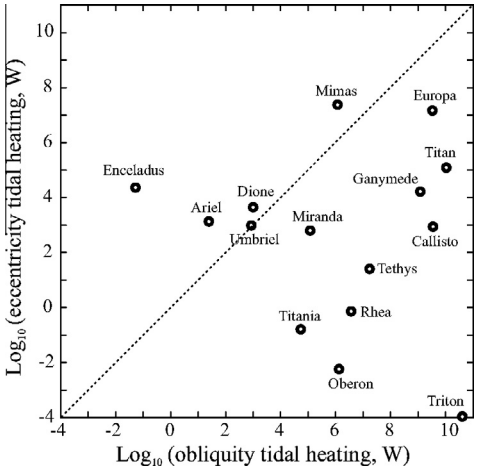

Fig. 4. Energy dissipated in various satellite oceans due to the obliquity and eccentricity tides calculated from the scalings summarized in Table 4. The parameters used are $h = 30$ km, $c_D = 0.002$, and satellite parameters from Table 2. For satellites lying to the right of the dotted line, the obliquity response is the dominant contribution to dissipation. Here for plotting purposes, Triton has energy dissipation associated with the eccentricity, but in reality, this value should be zero.

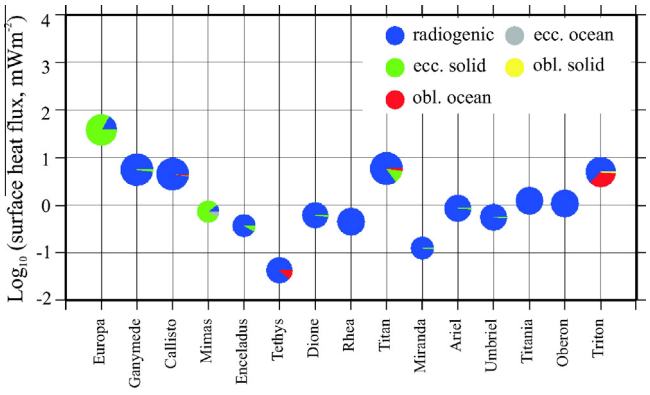

Fig. 5. Thermal heat budget for various outer Solar System satellites; solid body tidal heating components are calculated assuming a homogeneous elastic structure (Eq. (67)). Details of the calculations are presented in Section 5.1, while the numerical quantities are presented in Table 3. Pie charts indicate relative contributions from radiogenic heating (blue), solid body eccentricity tidal heating (green), solid body obliquity tidal heating (yellow), ocean obliquity tidal heating (red), and ocean eccentricity tidal heating (gray). The size of the pie charts are scaled by $\log(R)$. (For interpretation of the references to colour in this figure legend, the reader is referred to the web version of this article.)

decoupling ocean exists. In choosing the fluid and elastic limits, we likely bracket the actual value of the tidal dissipation, while providing insight into the degree of uncertainty associated with the tidal model. It is clear that for most of the satellites the thermal budgets are dominated by two components: radiogenic heating and eccentricity solid-body tidal heating. Triton and Tethys are likely the only satellites with large present-day heat contributions from obliquity tides, because of their relatively small eccentricities. Triton might be primarily heated by ocean obliquity tides, while Callisto and Titan could experience minor ocean heating.

5.2. Relative contributions from eccentricity and obliquity

While Tyler (2008, 2011) recognized that a satellite ocean response is typically dominated by the westward obliquity response, this is not always the case. Fig. 4 shows the energy dissipated in an ocean calculated with the input parameters $h = 30$ km, $c_D = 0.002$, and the satellite-appropriate parameters from Table 2. For most satellite oceans, the obliquity tidal heating contribution is larger than that from the eccentricity. The reason for this is twofold. First,

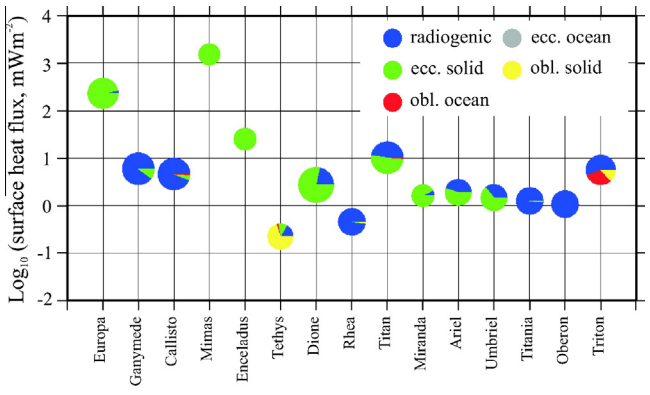

Fig. 6. Similar to Fig. 5, here with the solid body tidal heating components calculated assuming a completely fluid response ($k_2 = 3/2$).

assuming the obliquity response is in the low viscosity (nearly inviscid) regime, the average velocity will be much higher for the obliquity related flow due to the resonant response (Tyler, 2008),

if the obliquity and eccentricity are roughly comparable. Second, because higher velocities equate to higher effective viscosities (see Section 4.2), dissipation is further enhanced in the obliquity response.

Taking the scalings for the energy dissipation from Section 3.1 and Appendix F (summarized in Table 4) and the numerical results from Section 4.2, it can be shown, here in the low viscosity regime, that the obliquity likely dominates unless there is a significant disparity between the eccentricity and obliquity:

$$\frac{\dot{E}_{obl}}{\dot{E}_{ecc}} \approx \frac{44,800}{519}\left(\frac{1}{\epsilon}\right)^3\left(\frac{k_{obl}}{k_{ecc}}\right)\left(\frac{\theta_0}{e}\right)^3. \tag{71}$$

Recall that for these scalings to be applicable, the Lamb parameter, ϵ, must be low (30), and additionally, $\frac{k_{obl}}{k_{ecc}}$ is approximately 3 (cf. Section 4.2). Oceanic energy dissipation is clearly biased towards the obliquity response. Because of this, oceans on satellites with low orbital inclination, and thus, low Cassini state obliquity, are unlikely to experience significant dissipation (Chen and Nimmo, 2011).

5.3. Global tidal heating pattern

Thus far we have primarily discussed the time- and spatially-averaged energy dissipation rate. While this is an important quantity when thinking about the overall thermal and orbital evolution, the spatial distribution of tidal heat can also have implications for spacecraft observables. As suggested for solid-body tidal heating, spatial variations in the heat flux can generate lateral variations in conductive ice shell thickness (Ojakangas and Stevenson, 1989). These variations can potentially generate long-wavelength topography that can be detected through topography or gravity (Schenk and McKinnon, 2009; Nimmo and Bills, 2010). In addition, the spatial pattern of the heating at the base can affect convection in the ice shell (Tobie et al., 2005; Roberts and Nimmo, 2008). The effects of this convection may potentially manifest as geologic features on the surface (Tackley et al., 2001; Besserer et al., 2013).

We present the time-averaged global heating patterns in the ocean for the obliquity response and eccentricity response in Fig. 7. The primary power for both responses occurs in degrees $l = 0$, 2, and 4, as would be expected from tidally-driven flow. However the relative power in each degree and thus the location of hot and cold spots differ from the case for solid-body tidal heating (Ojakangas and Stevenson, 1989; Beuthe, 2013). In particular, ocean obliquity heating is maximized at the pole (as is solid-body eccentricity heating in a thin shell), while ocean eccentricity heating, although much smaller, is maximized at the equator. Obliquity tidal heating will thus tend to reinforce shell thickness variations arising because of solid-body eccentricity heating.

5.4. Triton

The thermal history of Triton is a puzzle; if satellite ocean tidal heating is significant for any icy satellite, it is most likely to be Triton. Observations of the surface features suggest that Triton has been quite active in the past (Smith, 1989; Croft et al., 1995; McKinnon and Kirk, 2007), and this activity could have been as recent as 10 Ma (Schenk and Zahnle, 2007). Eccentricity tides have been evoked for heating mechanisms like frictional shear heating (Prockter et al., 2005) or "thermal blanketing" (Gaeman et al., 2012), but because the eccentricity at present is zero, there is no clear reason why geologic activity should be recent. A significant amount of tidal heating likely occurred during Triton's capture and subsequent orbital circularization (Ross and Schubert, 1990); however, the likelihood that Triton's capture is recent is very low (Agnor and Hamilton, 2006; Schenk and Zahnle, 2007) and additionally, the circularization timescale, while dependent on the interior structure, is likely to be less than 1 Gyr (Ross and Schubert, 1990).

Prior to observations from *Voyager 2*, Jankowski et al. (1989) suggested that solid-body obliquity tidal heating could play a significant role in the thermal history of Triton, specifically if Triton occupied Cassini state 2. From imaging it was shown that this state was unlikely (Smith, 1989); however, the role of the obliquity tide on the evolution of Triton should not be discounted. Ultimately, the obliquity is related to the inclination of the orbit (Peale, 1969), and unlike eccentricity, the inclination is not damped rapidly (Murray and Dermott, 1999). It was recognized that the solid-body tidal heating contribution is small (Jankowski et al., 1989) if Triton is in Cassini state 1; however, the ocean can effectively contribute heat at a rate of approximately 66 GW if this is the case – comparable to radiogenic heat production (Figs. 5 and 6). Because the inclination has remained fairly constant, ocean tidal heating could have been involved throughout the thermal history of Triton, specifically aiding in keeping an ocean from freezing and providing a moderate heat source for recent geologic activity. Coupled thermal–orbital models that include ocean tidal heating could provide further insight into the long term evolution of Triton.

5.5. Caveats

In estimating the thermal budgets for the outer Solar System satellites (Figs. 5 and 6), we have used fairly simplistic models in order to calculate the amount of tidal dissipation both in the solid-body and ocean. These models are sufficient to capture and highlight broad trends. Given the general lack of data and large uncertainty in physical parameters, we do not attempt to carry

Table 4
Summary of scalings presented in Section 3 and Appendices E and F. Here we define: $u_0 = (\Omega^3 R^3)/(gh)$, $E_0 = \rho\Omega^6 R^8/(g^2 h)$ and $\dot{E}_0 = E_0 \nu/R^2$. These scalings are accurate to 10% of the full semi-analytic solution of Section 2.2 when $Re = \frac{\Omega R^2}{\nu} > 50$ and $\epsilon = \frac{4\Omega^2 R^2}{gh} \lesssim \frac{4}{15}$. The values presented for the coefficients in ν are numerically obtained (see Section 4.2).

Tidal component	Average velocity	Kinetic energy	$\dot{E}$	ν	Q
Obliquity-westward, $(\frac{1}{\epsilon Re} \ll \frac{1}{80})$	$\sqrt{\frac{3}{2}}\Omega R\theta_0$	$3\pi\rho h\Omega^2 R^4\theta_0^2$	$12\pi\rho h\Omega^2 R^2 \nu\theta_0^2$	–	$\frac{1}{4}Re$
Obliquity-westward, $(\frac{1}{\epsilon Re} \gtrsim \frac{1}{80})$	$\sqrt{\frac{3}{800}}u_0 Re\theta_0$	$\frac{3\pi}{400}E_0 Re^2\theta_0^2$	$\frac{3\pi}{100}\dot{E}_0 Re^2\theta_0^2$	–	
Obliquity-eastward	$\sqrt{\frac{2397}{54880}}u_0\theta_0$	$\frac{2397\pi}{27,440}E_0\theta_0^2$	$\frac{9237\pi}{6860}\dot{E}_0\theta_0^2$	–	$\frac{12,316}{799}Re$
Obliquity-general	$\sqrt{\frac{3}{2}}\frac{\Omega R\theta_0}{\left(1+\left[400\nu^2/u_0^2R^2\right]\right)^{1/2}}$	$\frac{3\pi\rho h\Omega^2R^4\theta_0^2}{(1+[400\nu^2/u_0^2R^2])}$	$\frac{12\pi\rho h\Omega^2R^2\nu\theta_0^2}{(1+[400\nu^2/u_0^2R^2])}$	$\frac{\Omega^3R^4}{20\sqrt{2}gh}\left(-1+\sqrt{1+\left[\frac{200}{3}\frac{0.40c_D g\theta_0}{\Omega^2R}\right]^2}\right)^{1/2}$	$\frac{1}{4}Re$
Eccentricity-radial	$\sqrt{\frac{57}{560}}u_0 e$	$\frac{57\pi}{280}E_0 e^2$	$\frac{39\pi}{14}\dot{E}_0 e^2$		$\frac{19}{260}Re$
Eccentricity-westward, librational	$\sqrt{\frac{3}{224}}u_0 e$	$\frac{3\pi}{112}E_0 e^2$	$\frac{69\pi}{140}\dot{E}_0 e^2$	–	$\frac{5}{92}Re$
Eccentricity-eastward, librational	$\sqrt{\frac{63}{160}}u_0 e$	$\frac{63\pi}{80}E_0 e^2$	$\frac{231\pi}{20}\dot{E}_0 e^2$	-	$\frac{3}{44}Re$
Eccentricity-total	–	$\frac{57\pi}{56}E_0 e^2$	$\frac{519\pi}{35}\dot{E}_0 e^2$	$0.13\frac{c_D\Omega^3R^5e}{gh^2}$	$\frac{95}{1384}Re$

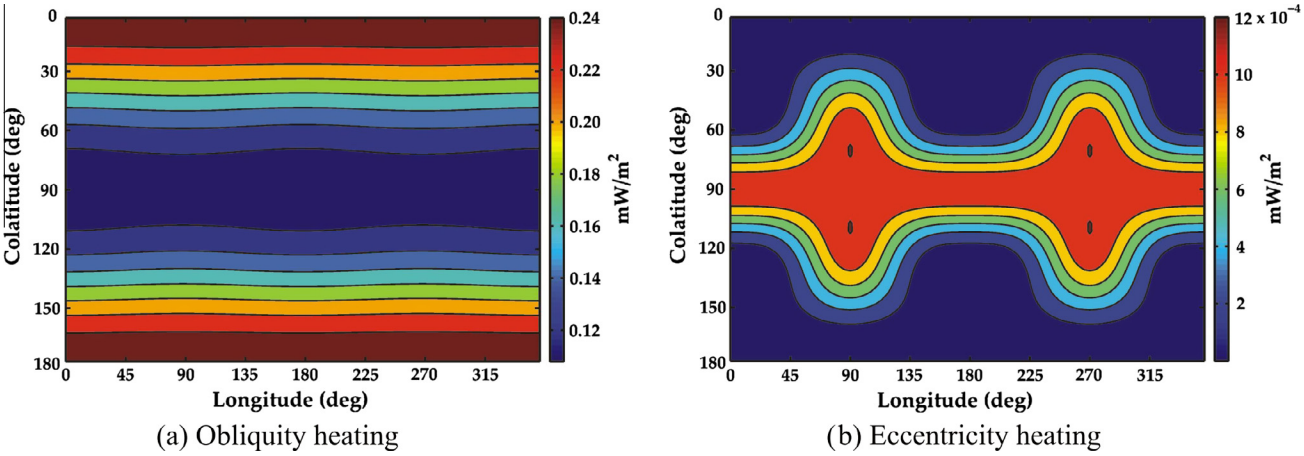

Fig. 7. Time-averaged energy dissipation pattern associated with (a) obliquity tidal response and (b) eccentricity tidal response for a model ocean on Europa. These are calculated from the numerical model presented in Section 4 with $c_D = 0.002$ and $h = 30$ km.

out models of specific bodies in this work. With regard to the solid body dissipation calculated here, it is recognized that the Maxwell viscoelastic model is insufficient to explain the tidal dissipation observed, for example for Enceladus (Meyer and Wisdom, 2007; Howett et al., 2011).

In adopting a simple model for the ocean behavior by analogy to Earth's oceans, we have neglected a significant dissipation mechanism, internal tides, which arise because of compositional stratification (Munk and MacDonald, 1960; Egbert and Ray, 2000). While Europa's ocean, at least, is electrically conductive, presumably due to brine (Khurana et al., 1998; Kargel et al., 2000), it is unclear whether satellite oceans are compositionally stratified (Goodman et al., 2004). The major drivers of compositional variations in Earth's oceans, such as evaporation or addition of fresh water, are likely much less important on icy satellites. Because internal tide generation is largely due to ocean bathymetry (Baines, 1973; Jayne and Laurent, 2001), a property which is completely unconstrained in the context of satellite oceans, we have ignored the effects of a stratified ocean. Additionally, our shallow-water approach cannot capture the effects of convection. Convection will alter the dynamics of the ocean flow to some extent (Chen et al., 2010; Soderlund et al., 2013). However, the magnitude of the tidally-driven velocities are likely comparable to those generated through convection and also, convection has a tendency to destroy stratification. Thus, the shallow-water model may be sufficient to predict the bulk satellite ocean behavior. Unfortunately, due to computational limitations, three-dimensional models that can include convection may not necessarily be more accurate than our shallow-water model, because these models are unable to resolve the processes that presumably dissipate energy in the system (Glatzmaier, 2002).

As discussed in Section 4, the appropriate value of the drag coefficient c_D is probably in the range 0.002–0.01. In using the lower bound, we are being conservative in our estimate of ocean heating. Similarly, our approach to calculating the obliquity θ_0 might be too low by a factor of $\approx$2 if decoupled shells are present (Section 5.1). Taken together, our ocean heating estimates could be low by at most a factor of 20. In most cases, this uncertainty would not change our conclusions – Mimas and Europa would join the existing candidates (Triton, Titan and Callisto) as possibly having experienced significant ocean obliquity heating.

Throughout this work, we assume a small Lamb parameter; the uncertainty in the Lamb parameter arises from the uncertainty in the ocean depth. The scalings we present in Section 3 are likely not applicable if the ocean depth is less than $\sim$10 km. However, if this is the case, the assumption of uniform ocean thickness in Eqs. (1) and (2) may also not be valid. Long-wavelength topography of either the ice shell above the ocean or the silicate mantle below the ocean can have amplitudes on the kilometer scale (Schenk and McKinnon, 2009; Nimmo and Bills, 2010). The dynamics of the ocean may be far more complex in the case of a very shallow ocean, and the shallow-water scalings we have described do not capture this complexity.

6. Conclusion

It was recognized by Tyler (2008, 2009, 2011) that tidal dissipation in a global ocean could provide a heat source that had not been previously recognized; however, the amount of dissipation could vary over orders of magnitude depending on the value of the effective viscosity (parameterized as either ν, α, or Q) implemented in the model. We have expanded that work in two ways. First, we provide scalings for the tidal responses, specifically the average kinetic energy and energy dissipation, in terms of the model input parameters. These can be easily implemented into thermal–orbital evolution models for many satellites, similar to relations used for solid-body tidal dissipation. Second and more importantly, we estimate the effective viscosity of a satellite global ocean based on analogy to frictional dissipation in oceans on Earth. Both of these results are summarized in Table 4.

Based on these scaling relations and estimates for the effective viscosity, we find that for almost all satellites the thermal budget is dominated by the radiogenic and solid-body eccentricity tidal heating, as long recognized. For completeness, evolution models can include ocean tidal dissipation; however, this is unlikely to create large deviations from previous results, unless high obliquities existed in the past. In the special case of Triton, ocean tidal heating may play a large role in keeping a primordial ocean warm, primarily because eccentricity tidal heating, either in the ocean or solid-body, is likely small after rapid circularization of the orbit post-capture. Because the inclination evolves on a much longer timescale than the eccentricity, obliquity tidal heating in the ocean can be significant even up to the present and may provide a heat source for the apparent recent geologic activity on the surface.

Acknowledgments

We thank Mikael Beuthe and Isamu Matsuyama for their thoughtful and thorough reviews. Chris Edwards and Doug Lin provided helpful insights and discussions. This work was supported by

NASA's Planetary Geology and Geophysics Program (NNZ09AD89G) and a UCSC Dissertation-Year Fellowship.

Appendix A. Useful spherical harmonic relations

To obtain equations for the spherical harmonic coefficients Ψ_l^m and Φ_l^m (e.g. Eqs. (21) and (22)), we used the following spherical harmonic relations:

$$Y_l^{-m} = (-1)^m Y_l^{m*}, \tag{A.1}$$

$$\nabla^2 Y_l^m = \frac{-l(l+1)}{R^2} Y_l^m, \tag{A.2}$$

$$\cos\theta Y_l^m = C_{l+1}^m Y_{l+1}^m + C_l^m Y_{l-1}^m, \tag{A.3}$$

$$\sin\theta \frac{\partial Y_l^m}{\partial \theta} = lC_{l+1}^m Y_{l+1}^m - (l+1) C_l^m Y_{l-1}^m. \tag{A.4}$$

These are similar to Eq. (3.17) of Longuet-Higgins (1968) and (23)–(25) of Tyler (2011) for normalized Laplace spherical harmonics. We use the convention that $\Psi_l^{-m} = (-1)^m \Psi_l^{m*}$ and likewise with η_l^{-m} and Φ_l^{-m}. In addition, a useful relation when calculating spatially averaged quantities, such as the kinetic energy, is

$$\int_0^{2\pi}\int_0^{\pi}\left[\frac{\partial Y_l^m}{\partial\theta}\frac{\partial Y_{l'}^{m'*}}{\partial\theta} + \frac{1}{\sin^2\theta}\frac{\partial Y_l^m}{\partial\phi}\frac{\partial Y_{l'}^{m'*}}{\partial\phi}\right]\sin\theta d\theta d\phi = l(l+1)\delta_{l,l'}\delta_{m,m'}. \tag{A.5}$$

Appendix B. Response to eastward propagating tidal potentials

In the linear system, we can separately solve for the response to the eastward propagating potentials. In this case, we seek wave solutions of the form:

$$\Psi(\theta,\phi,t) = \sum_{m=1}^{l}\sum_{l=1}^{\infty}\left[\Psi_l^m e^{-i\Omega t} Y_l^m + \Psi_l^{-m} e^{i\Omega t} Y_l^{-m}\right] = 2\Re\left(\sum_{m=1}^{l}\sum_{l=1}^{\infty}\left[\Psi_l^m e^{-i\Omega t} Y_l^m\right]\right) \tag{B.1}$$

and similarly for Φ and η.

The resulting coupled equations from substituting (B.1) and similar expressions for Φ and η into (16)–(18) are

$$\left[i\Omega - \alpha - \frac{\nu l(l+1)}{R^2} + \frac{2\Omega i m}{l(l+1)}\right]\Psi_l^m + 2\Omega\left[\frac{l-1}{l}C_l^m\Phi_{l-1}^m + \frac{l+2}{l+1}C_{l+1}^m\Phi_{l+1}^m\right] = 0, \tag{B.2}$$

$$\left[-i\Omega + \alpha + \frac{\nu l(l+1)}{R^2} - \frac{2\Omega i m}{l(l+1)} + \frac{igh l(l+1)}{\Omega R^2}\right]\Phi_l^m + 2\Omega\left[\frac{l-1}{l}C_l^m\Psi_{l-1}^m + \frac{l+2}{l+1}C_{l+1}^m\Psi_{l+1}^m\right] = -U_{2,E}^1\delta_{l,2}\delta_{m,1} - U_{2,E}^2\delta_{l,2}\delta_{m,2} \tag{B.3}$$

with the terms on the right hand side of (B.3) corresponding to the eastward obliquity tidal potential and eastward librational eccentricity tidal potential.

Appendix C. Response to the radial eccentricity tide

For the prior wave solutions (e.g. (19) and its equivalents or (B.1)), we have not included the $m = 0$ terms. The solutions for Ψ, Φ, and η must be real, and because the spherical harmonic Y_l^0 is real, the corresponding coefficients Ψ_l^0, Φ_l^0, and η_l^0 must be real. Because the linear system is separable in degree m, this only applies specifically for the radial component of the eccentricity forcing. To solve for this response, we can break the tidal potential (8) into a westward and eastward potential in a manner similar to that for the obliquity tide and librational component of the eccentricity tide with a constraint that the total response must be real, i.e.

$$\Psi(\theta,\phi,t) = \sum_{l=1}^{\infty}\left[\Psi_{l,W}^0 e^{i\Omega t} + \Psi_{l,E}^0 e^{-i\Omega t}\right]Y_l^0 \in \mathbb{R}, \tag{C.1}$$

and similarly for Φ and η. Here the coefficients are still complex and the subscripts W and E denoting the westward and eastward response, respectively. It can be shown that for (C.1) to be true, the relation

$$\Psi_{l,W}^0 = \left(\Psi_{l,E}^0\right)^*, \tag{C.2}$$

must be true, and similarly for Φ and η. We can solve either for the westward or eastward response, by substituting $-U_2^0\delta_{l,2}\delta_{m,0}$ for the right hand side of either (22) or (B.3) with the understanding that

$$\Psi(\theta,\phi,t) = \sum_{l=1}^{\infty}\left[\Psi_{l,W}^0 e^{i\Omega t} + \Psi_{l,E}^0 e^{-i\Omega t}\right]Y_l^0 = 2\sum_{l=1}^{\infty}\Re\left(\Psi_{l,W}^0 e^{i\Omega t}\right)Y_l^0 = 2\sum_{l=1}^{\infty}\Re\left(\Psi_{l,E}^0 e^{-i\Omega t}\right)Y_l^0 \tag{C.3}$$

and likewise for Φ and η.

Appendix D. Derived quantities

For ease of solution, the fluid dynamic equations are expressed in terms of the streamfunction Ψ and scalar potential Φ. However the quantities of interest are those such as kinetic energy or energy dissipation rate. Here we explicitly present the process to move from the spherical harmonic coefficients associated with the solution of the fluid dynamic equations to physical quantities.

D.1. Kinetic energy

Once the coefficients Ψ and Φ have been determined for the ocean response, the kinetic energy of the ocean flow, E_{tot}, can be calculated from

$$E_{tot} = \frac{\rho}{2}\int_V \vec{u}\cdot\vec{u}\, dV. \tag{D.1}$$

We ignore the potential energy contribution to the total energy because it is negligible when compared to this. The kinetic energy expressed in terms of Ψ and Φ is

$$E_{tot} = \frac{\rho}{2R^2}\int_V\left[\left(\frac{\partial\Phi}{\partial\theta} + \frac{1}{\sin\theta}\frac{\partial\Psi}{\partial\phi}\right)^2 + \left(\frac{1}{\sin\theta}\frac{\partial\Phi}{\partial\phi} - \frac{\partial\Psi}{\partial\theta}\right)^2\right]dV. \tag{D.2}$$

Because the energy is a nonlinear product, we must include both the westward and eastward responses, here denoted with the subscripts W and E, respectively. Expanding (D.2) in terms of the wave solutions from (19), its equivalents and (B.1) results in

$$E_{tot} = \frac{\rho h}{2}\int_0^{2\pi}\int_0^{\pi}\left\{\left[\sum_{m=1}^{l}\sum_{l=1}^{\infty}\left(\Phi_{l,W}^{m}e^{i\Omega t}\frac{\partial Y_l^m}{\partial\theta}+\Phi_{l,W}^{-m}e^{-i\Omega t}\frac{\partial Y_l^{-m}}{\partial\theta}\right.\right.\right.$$
$$+\Phi_{l,E}^{m}e^{-i\Omega t}\frac{\partial Y_l^m}{\partial\theta}+\Phi_{l,E}^{-m}e^{i\Omega t}\frac{\partial Y_l^{-m}}{\partial\theta}+\Psi_{l,W}^{m}e^{i\Omega t}\frac{1}{\sin\theta}\frac{\partial Y_l^m}{\partial\phi}$$
$$\left.+\Psi_{l,W}^{-m}e^{-i\Omega t}\frac{1}{\sin\theta}\frac{\partial Y_l^{-m}}{\partial\phi}+\Psi_{l,E}^{m}e^{-i\Omega t}\frac{1}{\sin\theta}\frac{\partial Y_l^m}{\partial\phi}+\Psi_{l,E}^{-m}e^{i\Omega t}\frac{1}{\sin\theta}\frac{\partial Y_l^{-m}}{\partial\phi}\right)\Bigg]^2$$
$$+\left[\sum_{m=1}^{l}\sum_{l=1}^{\infty}\left(\Phi_{l,W}^{m}e^{i\Omega t}\frac{1}{\sin\theta}\frac{\partial Y_l^m}{\partial\phi}+\Phi_{l,W}^{-m}e^{-i\Omega t}\frac{1}{\sin\theta}\frac{\partial Y_l^{-m}}{\partial\phi}\right.\right.$$
$$+\Phi_{l,E}^{m}e^{-i\Omega t}\frac{1}{\sin\theta}\frac{\partial Y_l^m}{\partial\phi}+\Phi_{l,E}^{-m}e^{i\Omega t}\frac{1}{\sin\theta}\frac{\partial Y_l^{-m}}{\partial\phi}-\Psi_{l,W}^{m}e^{i\Omega t}\frac{\partial Y_l^m}{\partial\theta}$$
$$\left.\left.\left.-\Psi_{l,W}^{-m}e^{-i\Omega t}\frac{\partial Y_l^{-m}}{\partial\theta}-\Psi_{l,E}^{m}e^{-i\Omega t}\frac{\partial Y_l^m}{\partial\theta}-\Psi_{l,E}^{-m}e^{i\Omega t}\frac{\partial Y_l^{-m}}{\partial\theta}\right)\right]^2\right\}\sin\theta d\theta d\phi. \quad (D.3)$$

By orthogonality of the spherical harmonics (5), the non-zero terms are

$$E_{tot} = \rho h\int_0^{2\pi}\int_0^{\pi}\left\{\sum_{m=1}^{l}\sum_{l=1}^{\infty}\left[\left(\Phi_{l,W}^{m}\Phi_{l,W}^{-m}+\Phi_{l,E}^{m}\Phi_{l,E}^{-m}+\Psi_{l,W}^{m}\Psi_{l,W}^{-m}+\Psi_{l,E}^{m}\Psi_{l,E}^{-m}\right.\right.\right.$$
$$\left.+\left(\Phi_{l,W}^{m}\Phi_{l,E}^{-m}+\Psi_{l,W}^{m}\Psi_{l,E}^{-m}\right)e^{i2\Omega t}+\left(\Phi_{l,E}^{m}\Phi_{l,W}^{-m}+\Psi_{l,E}^{m}\Psi_{l,W}^{-m}\right)e^{-i2\Omega t}\right)$$
$$\left.\left.\times\left(\frac{\partial Y_l^m}{\partial\theta}\frac{\partial Y_l^{-m}}{\partial\theta}+\frac{1}{\sin^2\theta}\frac{\partial Y_l^m}{\partial\phi}\frac{\partial Y_l^{-m}}{\partial\phi}\right)\right]\right\}\sin\theta d\theta d\phi. \quad (D.4)$$

Substituting (A.5) into (D.4) and averaging over an orbital period, we find that the average kinetic energy is

$$E_{tot,avg} = \rho h\sum_{l=1}^{\infty}\sum_{m=1}^{l}l(l+1)\left(\left|\Phi_{l,W}^{m}\right|^2+\left|\Phi_{l,E}^{m}\right|^2+\left|\Psi_{l,W}^{m}\right|^2+\left|\Psi_{l,E}^{m}\right|^2\right), \quad (D.5)$$

where the time-dependent components of (D.4) integrate to zero. This expression makes physical sense: the kinetic energy of the flow depends on the amplitude of the tidal response, but not on the phase.

While (D.1) is nonlinear, the solution is separable in m. For ease in presentation, we calculate the $m = 0$ component separately. The kinetic energy Eq. (D.2) can be expanded further in terms of the radial response from (C.3) resulting in

$$E_{tot}^{0} = \frac{\rho h}{2}\int_0^{2\pi}\int_0^{\pi}\left\{\left[\sum_{l=1}^{\infty}\left(\Phi_{l,W}^{0}e^{i\Omega t}+\Phi_{l,W}^{0*}e^{-i\Omega t}\right)\frac{\partial Y_l^0}{\partial\theta}\right]^2\right.$$
$$\left.+\left[-\sum_{l=1}^{\infty}\left(\Psi_{l,W}^{0}e^{i\Omega t}+\Psi_{l,W}^{0*}e^{-i\Omega t}\right)\frac{\partial Y_l^0}{\partial\theta}\right]^2\right\}\sin\theta d\theta d\phi. \quad (D.6)$$

From the relation (A.5), the non-trivial terms of (D.6) are

$$E_{rad,tot} = \frac{\rho h}{2}\sum_{l=1}^{\infty}(l)(l+1)$$
$$\left[\left(\Phi_{l,W}^{0}e^{i\Omega t}+\Phi_{l,W}^{0*}e^{-i\Omega t}\right)^2+\left(\Psi_{l,W}^{0}e^{i\Omega t}+\Psi_{l,W}^{0*}e^{-i\Omega t}\right)^2\right] \quad (D.7)$$

which include both time-dependent and time-independent terms. When averaged over the orbital period, the kinetic energy associated with the radial response is

$$E_{rad,tot,avg}^{0} = \rho h\sum_{l=1}^{\infty}l(l+1)\left(\left|\Phi_{l,W}^{0}\right|^2+\left|\Psi_{l,W}^{0}\right|^2\right). \quad (D.8)$$

The sum of (D.5) and (D.8) is presented in (24).

D.2. Energy dissipation

Additionally, the amount of energy dissipation is related to the flow response. Integrated over an orbital period, the amount of work done by the tides should be equivalent to the amount of frictional energy dissipated in the ocean. To calculate these quantities, we can take the time-averaged volumetric integral of the scalar product of the momentum equation and the horizontal velocity vector. In this section, we present the calculation of both of these quantities; the calculation for viscous dissipation is far more straightforward, while the calculation of the tidal work provides more physical insight. We consider the two linear models for viscous dissipation presented in (1).

D.2.1. Viscous dissipation in the ocean

The energy dissipated in the ocean is dependent on the viscous term employed. Tyler (2011) employs a linear drag (Rayleigh dissipation) formulation, in which the global dissipation rate is given by

$$\dot{E}_{lin} = \rho\int_V(\alpha\vec{u}\cdot\vec{u})dV. \quad (D.9)$$

where here we take the dissipation to be positive. This essentially scales with the kinetic energy given by (D.1). Averaged over an orbital period (cf. (24)), the viscous dissipation in terms of Ψ and Φ is

$$\dot{E}_{lin,avg} = 2\alpha E_{tot,avg} = 2\alpha\rho h\left[\sum_{l=1}^{\infty}l(l+1)\left(\left|\Phi_{l,W}^{0}\right|^2+\left|\Psi_{l,W}^{0}\right|^2\right)\right.$$
$$\left.+\sum_{l=1}^{\infty}\sum_{m=1}^{l}l(l+1)\left(\left|\Phi_{l,W}^{m}\right|^2+\left|\Phi_{l,E}^{m}\right|^2+\left|\Psi_{l,W}^{m}\right|^2+\left|\Psi_{l,E}^{m}\right|^2\right)\right]. \quad (D.10)$$

For a Navier–Stokes type viscosity, the solution to the integral

$$\dot{E}_{NS} = -\rho\int_V[(\nu\nabla^2\vec{u})\cdot\vec{u}]dV \quad (D.11)$$

is also similar to (D.1) with an additional prefactor of $-l(l+1)/R^2$ introduced to the summation by the Laplacian operator. The associated time-averaged energy dissipation is thus,

$$\dot{E}_{NS,avg} = \frac{2\rho h\nu}{R^2}\left[\sum_{l=1}^{\infty}l^2(l+1)^2\left(\left|\Phi_{l,W}^{0}\right|^2+\left|\Psi_{l,W}^{0}\right|^2\right)\right.$$
$$\left.+\sum_{l=1}^{\infty}\sum_{m=1}^{l}l^2(l+1)^2\left(\left|\Phi_{l,W}^{m}\right|^2+\left|\Phi_{l,E}^{m}\right|^2+\left|\Psi_{l,W}^{m}\right|^2+\left|\Psi_{l,E}^{m}\right|^2\right)\right]. \quad (D.12)$$

D.2.2. Work done by the tide

The work done by the tidal potential can be calculated from

$$\dot{E} = -\rho\int_V(\nabla U\cdot\vec{u})dV = -\rho h\int_S(\nabla U\cdot\vec{u})dS$$
$$= -\rho hR^2\int_0^{2\pi}\times\int_0^{\pi}\left[\left(\frac{1}{R}\frac{\partial U}{\partial\theta}\right)u_\theta+\left(\frac{1}{R\sin\theta}\frac{\partial U}{\partial\phi}\right)u_\phi\right]\sin\theta d\theta d\phi, \quad (D.13)$$

The full tidal potential U is the sum of each of the components presented in Section 2.1,

$$U = U_2^0(e^{i\Omega t}+e^{-i\Omega t})Y_2^0$$
$$+U_{2,W}^1\left(e^{i\Omega t}Y_2^1-e^{-i\Omega t}Y_2^{-1}+e^{-i\Omega t}Y_2^1-e^{i\Omega t}Y_2^{-1}\right)$$
$$+U_{2,W}^2\left(e^{i\Omega t}Y_2^2+e^{-i\Omega t}Y_2^{-2}\right)+U_{2,E}^2\left(e^{-i\Omega t}Y_2^2+e^{i\Omega t}Y_2^{-2}\right). \quad (D.14)$$

Similar to (D.1), the integral (D.13) is separable in m. Therefore, for clarity, we present the dissipation associated with radial component ($m = 0$) separately.

For the obliquity tide and the librational components of the eccentricity tide, the integral (D.13) in terms of the tidal potentials and response coefficients is

$$\dot{E}=-\rho h\int_0^{2\pi}\int_0^{\pi}\left\{\left[\sum_{m=1}^{2}\left(U^m_{2,W}e^{i\Omega t}\frac{\partial Y^m_2}{\partial\theta}+U^{-m}_{2,W}e^{-i\Omega t}\frac{\partial Y^{-m}_2}{\partial\theta}+U^m_{2,E}e^{-i\Omega t}\frac{\partial Y^m_2}{\partial\theta}+U^{-m}_{2,E}e^{i\Omega t}\frac{\partial Y^{-m}_2}{\partial\theta}\right)\right]\right.$$
$$\times\left[\sum_{l=1}^{\infty}\sum_{m=1}^{l}\left(\Phi^m_{l,W}e^{i\Omega t}\frac{\partial Y^m_l}{\partial\theta}+\Phi^{-m}_{l,W}e^{-i\Omega t}\frac{\partial Y^{-m}_l}{\partial\theta}+\Psi^m_{l,W}e^{i\Omega t}\frac{1}{\sin\theta}\frac{\partial Y^m_l}{\partial\phi}+\Psi^{-m}_{l,W}e^{-i\Omega t}\frac{1}{\sin\theta}\frac{\partial Y^{-m}_l}{\partial\phi}\right.\right.$$
$$\left.\left.+\Phi^m_{l,E}e^{-i\Omega t}\frac{\partial Y^m_l}{\partial\theta}+\Phi^{-m}_{l,E}e^{i\Omega t}\frac{\partial Y^{-m}_l}{\partial\theta}+\Psi^m_{l,E}e^{-i\Omega t}\frac{1}{\sin\theta}\frac{\partial Y^m_l}{\partial\phi}+\Psi^{-m}_{l,E}e^{i\Omega t}\frac{1}{\sin\theta}\frac{\partial Y^{-m}_l}{\partial\phi}\right)\right]$$
$$+\left[\sum_{m=1}^{2}\left(U^m_{2,W}e^{i\Omega t}\frac{1}{\sin\theta}\frac{\partial Y^m_2}{\partial\phi}+U^{-m}_{2,W}e^{-i\Omega t}\frac{1}{\sin\theta}\frac{\partial Y^{-m}_2}{\partial\phi}+U^m_{2,E}e^{-i\Omega t}\frac{1}{\sin\theta}\frac{\partial Y^m_2}{\partial\phi}+U^{-m}_{2,E}e^{i\Omega t}\frac{1}{\sin\theta}\frac{\partial Y^{-m}_2}{\partial\phi}\right)\right]$$
$$\times\left[\sum_{l=1}^{\infty}\sum_{m=1}^{l}\left(\Phi^m_{l,W}e^{i\Omega t}\frac{1}{\sin\theta}\frac{\partial Y^m_l}{\partial\phi}+\Phi^{-m}_{l,W}e^{-i\Omega t}\frac{1}{\sin\theta}\frac{\partial Y^{-m}_l}{\partial\phi}-\Psi^m_{l,W}e^{i\Omega t}\frac{\partial Y^m_l}{\partial\theta}-\Psi^{-m}_{l,W}e^{-i\Omega t}\frac{\partial Y^{-m}_l}{\partial\theta}\right.\right.$$
$$\left.\left.\left.+\Phi^m_{l,E}e^{-i\Omega t}\frac{1}{\sin\theta}\frac{\partial Y^m_l}{\partial\phi}+\Phi^{-m}_{l,E}e^{i\Omega t}\frac{1}{\sin\theta}\frac{\partial Y^{-m}_l}{\partial\phi}-\Psi^m_{l,E}e^{-i\Omega t}\frac{\partial Y^m_l}{\partial\theta}-\Psi^{-m}_{l,E}e^{i\Omega t}\frac{\partial Y^{-m}_l}{\partial\theta}\right)\right]\right\}\sin\theta d\theta d\phi. \tag{D.15}$$

Using the relation (5), the non-trivial components of (D.15) are

$$\dot{E}=-\rho h\int_0^{2\pi}\int_0^{\pi}\left[\sum_{m=1}^{2}\left(U^m_{2,W}\Phi^{-m}_{2,W}+U^{-m}_{2,W}\Phi^m_{2,W}+U^m_{2,E}\Phi^{-m}_{2,E}+U^{-m}_{2,E}\Phi^m_{2,E}\right.\right.$$
$$+\left(U^m_{2,W}\Phi^{-m}_{2,E}+U^{-m}_{2,E}\Phi^m_{2,W}\right)e^{i2\Omega t}+\left(U^m_{2,E}\Phi^{-m}_{2,W}+U^{-m}_{2,W}\Phi^m_{2,E}\right)e^{-i2\Omega t}$$
$$\left.\left.\times\left(\frac{\partial Y^m_l}{\partial\theta}\frac{\partial Y^{-m}_l}{\partial\theta}+\frac{1}{\sin^2\theta}\frac{\partial Y^m_l}{\partial\phi}\frac{\partial Y^{-m}_l}{\partial\phi}\right)\right]\sin\theta d\theta d\phi. \tag{D.16}$$

Making use of (A.5) and recalling that the coefficients describing the tides (e.g. $U^1_{2,W}$) are real, (D.16) simplifies to

$$\dot{E}=-2(2)(3)\rho h\sum_{m=1}^{2}\left(U^m_{2,W}\Re\left(\Phi^m_{2,W}\right)+U^m_{2,E}\Re\left(\Phi^m_{2,E}\right)\right.$$
$$\left.+\left(U^m_{2,W}\Phi^{m*}_{2,E}+U^m_{2,E}\Phi^m_{2,W}\right)e^{i2\Omega t}+\left(U^m_{2,E}\Phi^{m*}_{2,W}+U^m_{2,W}\Phi^m_{2,E}\right)e^{-i2\Omega t}\right). \tag{D.17}$$

Thus, the time-averaged tidal dissipation for the obliquity and librational tides is

$$\dot{E}_{avg}=-2(2)(3)\rho h\sum_{m=1}^{2}\left(U^m_{2,W}\Re\left(\Phi^m_{2,W}\right)+U^m_{2,E}\Re\left(\Phi^m_{2,E}\right)\right). \tag{D.18}$$

The dissipation associated with the radial component is given by

$$\dot{E}_{rad}=-\rho h\int_0^{2\pi}\int_0^{\pi}\left\{\left(U^0_2(e^{i\Omega t}+e^{-i\Omega t})\frac{\partial Y^0_2}{\partial\theta}\right)\right.$$
$$\left.\left[\sum_{l=1}^{\infty}\left(\left(\Phi^0_{l,W}e^{i\Omega t}+\Phi^{0*}_{l,W}e^{-i\Omega t}\right)\frac{\partial Y^0_l}{\partial\theta}\right)\right]\right\}\sin\theta d\theta d\phi. \tag{D.19}$$

The solution of (D.19) can be used to derive a time-averaged dissipation of

$$\dot{E}_{rad,avg}=-2(3)\rho hU^0_2\left(\Phi^0_{2,W}+\Phi^{0*}_{2,W}\right)$$
$$=-2(2)(3)\rho hU^0_2\Re\left(\Phi^0_{2,W}\right). \tag{D.20}$$

The sum of (D.18) and (D.20) is presented in (28).

Appendix E. Scalings for the response to the eastward obliquity tide

While the magnitudes of the forcing potentials for the eastward and westward propagating obliquity tides are the same, the response of the ocean is fundamentally different. For the westward response, the kinetic energy and energy dissipation are dominated by the lowest mode, $|\Psi^1_1|$. For the eastward response, the kinetic energy is significant in the lowest three modes with the largest amplitude being $|\Phi^1_2|$ (see Fig. 1). There only exists a single scaling regime, and the approximations made here break down at small Reynolds numbers (see criteria given in (29)).

The vorticity Eq. (B.2) provides the relationships between Ψ^1_1, Ψ^1_3 and Φ^1_2, here assuming power existing only in the three largest modes and expressed in terms of the Reynolds number:

$$\Psi^1_1=\frac{3}{2}\frac{C^1_2}{\left(\left(\frac{1}{Re}\right)^2+1\right)}\left(\frac{1}{Re}+i\right)\Phi^1_2 \tag{E.1}$$

and

$$\Psi^1_3\approx\frac{4}{3}\frac{C^1_3}{\left(\left(\frac{12}{Re}\right)^2+\frac{49}{36}\right)}\left(\frac{12}{Re}+i\frac{7}{6}\right)\Phi^1_2. \tag{E.2}$$

The response coefficients are related to the forcing potential through the horizontal divergence of the momentum Eq. (B.3), here written in terms of Reynolds number and Lamb parameter,

$$\left[-i\frac{4}{3}+i\frac{24}{\epsilon}+\frac{6}{Re}\right]\Phi^1_2+C^1_2\Psi^1_1+\frac{8}{3}C^1_3\Psi^1_3\approx\frac{-U^1_{2,W}}{\Omega}. \tag{E.3}$$

For large Re, the Reynolds number terms in the denominator of (E.1) and (E.2) can be neglected. The dominant terms of (E.3) are

$$\left[\frac{6}{Re}+\frac{3}{2}\frac{\left(C^1_2\right)^2}{Re}+\frac{1536}{49}\frac{\left(C^1_3\right)^2}{Re}+i\frac{24}{\epsilon}\right]\Phi^1_2$$
$$=\left[\frac{9237}{686}\left(\frac{1}{Re}\right)+i\frac{24}{\epsilon}\right]\Phi^1_2\approx\frac{-U^1_{2,W}}{\Omega}, \tag{E.4}$$

after making the substitutions for Ψ^1_1 and Ψ^1_3 and neglecting their imaginary components for small Lamb parameter. The resulting flow is given by

$$\left|\Phi^1_2\right|\approx\left|\Im\left(\Phi^1_2\right)\right|\approx\frac{U^1_{2,W}\epsilon}{24\Omega}=\frac{1}{4}\sqrt{\frac{2\pi}{15}}\frac{\Omega^3R^4\theta_0}{gh}, \tag{E.5}$$

$$\left|\Psi^1_1\right|\approx\left|\Im\left(\Psi^1_1\right)\right|\approx\frac{3}{2}C^1_2\left|\Phi^1_2\right|=\frac{3}{2\sqrt{5}}\left|\Phi^1_2\right|, \tag{E.6}$$

$$\left|\Psi^1_3\right|\approx\left|\Im\left(\Psi^1_3\right)\right|\approx\frac{8}{7}C^1_3\left|\Phi^1_2\right|=\frac{8}{7}\sqrt{\frac{8}{35}}\left|\Phi^1_2\right|. \tag{E.7}$$

Combining (E.5) with the relations (E.6) and (E.7) and the kinetic energy Eq. (24), we find that the kinetic energy is independent of viscosity,

$$E_{tot,obl,E}\approx\rho h\left[2\left|\Psi^1_1\right|^2+6\left|\Phi^1_2\right|^2+12\left|\Psi^1_3\right|^2\right]$$
$$\approx\rho h\left[\frac{9}{10}\left|\Phi^1_2\right|^2+6\left|\Phi^1_2\right|^2+\frac{6144}{1715}\left|\Phi^1_2\right|^2\right]$$
$$=\rho h\left(\frac{7191}{686}\right)\left|\Phi^1_2\right|^2\approx\frac{2397\pi}{27,440}\frac{\rho\Omega^6R^8\theta_0^2}{g^2h}. \tag{E.8}$$

The kinetic energy in turn may be used to determine an averaged flow speed $\bar{u}$:

$$\bar{u}\approx\sqrt{\frac{2397}{54,880}}\frac{\Omega^3R^3\theta_0}{gh}. \tag{E.9}$$

The associated energy dissipation calculated from (28) and the solution of (E.4) is given by

$$\dot{E}=-12\rho hU^1_{2,W}\Re\left(\Phi^1_{2,E}\right)$$
$$\approx-12\rho hU^1_{2,W}\left(\frac{-3079}{131,712}\left(\frac{U^1_{2,W}\epsilon^2}{\Omega Re}\right)\right)$$
$$=\frac{9237\pi}{6860}\frac{\rho\Omega^6R^6\nu\theta_0^2}{g^2h}. \tag{E.10}$$

The tidal quality factor as defined by (51) is

$$Q_{obl,E} = \frac{\Omega \dot{E}_{obl,E}}{E_{tot,obl,E}} \approx \frac{\Omega\left(\frac{9237\pi}{6860}\frac{\rho\Omega^6 R^6 \nu\theta_0^2}{g^2 h}\right)}{\left(\frac{2397\pi}{27,440}\frac{\rho\Omega^6 R^8 \theta_0^2}{g^2 h}\right)} = \frac{12,316}{799}\left(\frac{\Omega R^2}{\nu}\right) = \frac{12,316}{799} Re. \tag{E.11}$$

E.1. Relative contribution from eastward obliquity

Throughout this paper, we have ignored the response to the eastward propagating obliquity tide. Under the assumptions of high Reynolds number and low Lamb parameter, it can be formally shown that the contribution from the eastward obliquity response is negligible when compared to that of the westward propagating response.

In the high Reynolds number regime, the kinetic energy ratio is independent of the ocean viscosity. From Section 3.1 and Appendix E, the relative contributions to the kinetic energy from the westward and eastward obliquity responses are

$$\frac{E_{tot,W}}{E_{tot,E}} \approx \frac{3\pi\rho h\Omega^2 R^4 \theta_0^2}{\frac{2397\pi}{27,440}\frac{\rho\Omega^6 R^8 \theta_0^2}{g^2 h}} = \frac{439,040}{799}\left(\frac{1}{\epsilon}\right)^2 \gtrsim 7700. \tag{E.12}$$

In the low Reynolds number regime, this ratio is sensitive to the Reynolds number with

$$\frac{E_{tot,W}}{E_{tot,E}} \approx \frac{\frac{3\pi}{400}\frac{\rho\Omega^8 R^{12}\theta_0^2}{\nu^2 g^2 h}}{\frac{2397\pi}{27,440}\frac{\rho\Omega^6 R^8 \theta_0^2}{g^2 h}} = \frac{343}{495} Re^2 \gtrsim 1700. \tag{E.13}$$

Similarly, the ratio of energy dissipation is independent of viscosity in the high Reynolds number regime,

$$\frac{\dot{E}_{obl,W}}{\dot{E}_{obl,E}} \approx \frac{12\pi\rho h\Omega^2 R^2 \nu\theta_0^2}{\frac{9237\pi}{6860}\frac{\rho\Omega^6 R^6 \nu\theta_0^2}{g^2 h}} = \frac{439,040}{3079}\left(\frac{1}{\epsilon}\right)^2 \gtrsim 2000 \tag{E.14}$$

and scales inversely with the Reynolds number in the low Reynolds number regime,

$$\frac{\dot{E}_{obl,W}}{\dot{E}_{obl,E}} \approx \frac{\frac{3\pi}{100}\frac{\rho\Omega^8 R^{10}\theta_0^2}{\nu g^2 h}}{\frac{9237\pi}{6860}\frac{\rho\Omega^6 R^6 \nu\theta_0^2}{g^2 h}} = \frac{343}{15,395} Re^2 \gtrsim 55. \tag{E.15}$$

Typical satellite parameters (e.g. Tables 1 and 2) usually lie far from the scaling limits used to calculate these ratios, and the ratios presented in Eqs. (E.12)–(E.14) and (E.15) are typically much lower than those for actual satellite parameters. Therefore, we reasonably ignore the contribution of the eastward obliquity response in all obliquity-related scalings.

Appendix F. Scalings for the response to the eccentricity tide

The responses to the eccentricity tide is similar to that of the eastward propagating obliquity tide, in that there is a single scaling regime characterized by a kinetic energy profile that is independent of viscosity and energy dissipation linearly varying with viscosity. Unlike the unequal responses of the eastward and westward propagating obliquity tide, the magnitudes of the responses to each of the three components of the eccentricity tide are comparable. We present scalings for each tidal component separately, as well as including scalings for the total response.

F.1. Scalings for the response to the radial eccentricity tide

The response to the radial eccentricity tidal potential can be approximated with the lowest three modes, $\Psi_1^0, \Phi_2^0, \Psi_3^0$. From (21) and ignoring the contributions from the Reynolds number terms in the denominator, similar to the process used in Appendix E, the relations between the three modes are

$$\Psi_1^0 \approx 3C_2^0\left(\frac{2}{Re} - i\right)\Phi_2^0 \tag{F.1}$$

and

$$\Psi_3^0 \approx \frac{4}{3}C_3^0\left(\frac{12}{Re} - i\right)\Phi_2^0 \tag{F.2}$$

These modes are related to the tidal forcing by

$$\left[i + \frac{6}{Re} - \frac{i24}{\epsilon} + 2\left(\frac{C_2^0}{2}\right)\left(3C_2^0\left(\frac{2}{Re} - i\right)\right) + 2\left(\frac{4C_3^0}{3}\right)\left(\frac{4}{3}C_3^0\left(\frac{12}{Re} - i\right)\right)\right]\Phi_2^0 \approx \frac{-U_2^0}{\Omega}, \tag{F.3}$$

where the dominant real and imaginary terms end up being

$$\left[\frac{130}{7}\left(\frac{1}{Re}\right) - \frac{i24}{\epsilon}\right]\Phi_2^0 \approx \frac{-U_2^0}{\Omega}. \tag{F.4}$$

The forced response $|\Phi_2^0|$ is thus,

$$|\Phi_2^0| \approx \left|\Im\left(\Phi_2^0\right)\right| \approx \frac{U_2^0 \epsilon}{24\Omega} = \frac{1}{4}\sqrt{\frac{\pi}{5}}\frac{\Omega^3 R^4 e}{gh}. \tag{F.5}$$

For large Reynolds numbers, the relations (F.1) and (F.2) are dominated by the imaginary term, such that

$$|\Psi_1^0| \approx \left|\Im\left(\Psi_1^0\right)\right| \approx 3C_2^0|\Phi_2^0| = 3\sqrt{\frac{4}{15}}|\Phi_2^0|, \tag{F.6}$$

and

$$|\Psi_3^0| \approx |\Im(\Psi_3^0)| \approx \frac{4}{3}C_3^0|\Phi_2^0| = 4\sqrt{\frac{1}{35}}|\Phi_2^0|. \tag{F.7}$$

Using the lowest three modes, the average kinetic energy associated with the radial tide can be approximated from (24) as

$$E_{tot,rad} \approx \rho h\left[2\left|\Psi_1^0\right|^2 + 6\left|\Phi_2^0\right|^2 + 12\left|\Psi_3^0\right|^2\right]. \tag{F.8}$$

Combining the relations (F.1), (F.2) and (F.5) with (F.8), we find that the average kinetic energy is

$$E_{tot,rad} \approx \rho h\left[2\left(3C_2^0|\Phi_2^0|\right)^2 + 6|\Phi_2^0|^2 + 12\left(\frac{4}{3}C_3^0|\Phi_2^0|\right)^2\right] = \rho h\left[\frac{114}{7}|\Phi_2^0|^2\right] \approx \frac{57\pi}{280}\frac{\rho\Omega^6 R^8 e^2}{g^2 h}, \tag{F.9}$$

and thus the associated average velocity is given by

$$\bar{u} \approx \sqrt{\frac{57}{560}}\frac{\Omega^3 R^3 e}{gh}. \tag{F.10}$$

From (F.4), we can also calculate $\Re\left(\Phi_2^0\right)$,

$$\Re(\Phi_2^0) \approx \frac{-U_2^0}{\Omega\left(\frac{24}{\epsilon}\right)^2}\left(\frac{130}{7}\left(\frac{1}{Re}\right)\right) = \frac{-65}{84}\sqrt{\frac{\pi}{5}}\frac{\Omega^4 R^4 \nu e}{g^2 h^2}. \tag{F.11}$$

The resulting dissipation from (D.20) is thus

$$\dot{E}_{rad} \approx -12\rho h U_2^0 \Re\left(\Phi_2^0\right) \approx \frac{39\pi}{14}\frac{\rho\Omega^6 R^6 \nu e^2}{g^2 h}. \tag{F.12}$$

Combining (F.9) and (F.12), we find that the tidal quality factor associated with the radial response is

$$Q_{rad} \approx \frac{\Omega\left(\frac{57\pi}{280}\frac{\rho\Omega^6R^8e^2}{g^2h}\right)}{\frac{39\pi}{14}\frac{\rho\Omega^6R^6\nu e^2}{g^2h}} = \frac{19}{260}\left(\frac{\Omega R^2}{\nu}\right) = \frac{19}{260}Re. \quad \text{(F.13)}$$

F.2. Scalings for the response to the westward propagating component of the librational eccentricity tide

The response of the ocean to the librational eccentricity tidal potential is dominated by the lowest two modes, Φ_2^2 and Ψ_3^2. To calculate the westward response, we return to the vorticity equation given by (21). It can be shown that for large Reynolds numbers

$$\Psi_3^2 \approx 3C_3^2\left(\frac{12}{Re} - i\frac{2}{3}\right)\Phi_2^2 \quad \text{(F.14)}$$

and

$$|\Psi_3^2| \approx |\Im(\Psi_3^2)| \approx 2C_3^2|\Phi_2^2| = 2\sqrt{\frac{1}{7}}|\Phi_2^2|. \quad \text{(F.15)}$$

From (22) and including the dominant real and imaginary terms as before, the tidal response is given by

$$\left[\frac{6}{Re} + \frac{96\left(C_3^2\right)^2}{Re} - i\frac{24}{\epsilon}\right]\Phi_2^2 = \left[\frac{138}{7}\left(\frac{1}{Re}\right) - i\frac{24}{\epsilon}\right]\Phi_2^2 \approx \frac{-U_{2,W}^2}{\Omega}. \quad \text{(F.16)}$$

Similar to the response to the radial component, the kinetic energy is related to

$$|\Phi_2^2| \approx \left|\Im\left(\Phi_2^2\right)\right| \approx \frac{\left|U_{2,W}^2\right|\epsilon}{24\Omega} = \frac{1}{8}\sqrt{\frac{2\pi}{15}}\frac{\Omega^3R^4e}{gh} \quad \text{(F.17)}$$

while the dissipation is related to

$$\Re\left(\Phi_2^2\right) \approx \frac{-U_{2,W}^2}{\Omega\left(\frac{24}{\epsilon}\right)^2}\left(\frac{138}{7}\left(\frac{1}{Re}\right)\right) = \frac{-23}{56}\sqrt{\frac{2\pi}{15}}\left(\frac{\Omega^4R^4\nu e}{g^2h^2}\right). \quad \text{(F.18)}$$

The average kinetic energy associated with the response can be approximated from (24), (F.15) and (F.17) as

$$\begin{aligned} E_{tot,lib,W} &\approx \rho h\left[6|\Phi_2^2|^2 + 12|\Psi_3^2|^2\right] \\ &\approx \rho h\left[6|\Phi_2^2|^2 + 12\left(2C_3^2|\Phi_2^2|\right)^2\right] = \rho h\left[\frac{90}{7}|\Phi_2^2|^2\right] \\ &\approx \frac{3\pi}{112}\frac{\rho\Omega^6R^8e^2}{g^2h} \end{aligned} \quad \text{(F.19)}$$

with a corresponding average flow speed of

$$\bar{u} \approx \sqrt{\frac{3}{224}}\frac{\Omega^3R^3e}{gh}. \quad \text{(F.20)}$$

From the relations (28) and (F.18), the associated energy dissipation is

$$\dot{E}_{lib,W} \approx -12\rho h U_{2,W}^2\Re\left(\Phi_{2,W}^2\right) \approx \frac{69\pi}{140}\frac{\rho\Omega^6R^6\nu e^2}{g^2h}. \quad \text{(F.21)}$$

The associated Q is therefore

$$Q_{lib,W} \approx \frac{\Omega\left(\frac{3\pi}{112}\frac{\rho\Omega^6R^8e^2}{g^2h}\right)}{\left(\frac{69\pi}{140}\frac{\rho\Omega^6R^6\nu e^2}{g^2h}\right)} = \frac{5}{92}\left(\frac{\Omega R^2}{\nu}\right) = \frac{5}{92}Re. \quad \text{(F.22)}$$

F.3. Scalings for the response to the eastward propagating component of the librational eccentricity tide

The process to calculate the response to the eastward propagating librational component of the eccentricity tide is essentially the same as that for the westward response. The relationship between Φ_2^2 and Ψ_3^2 as given by (B.2) is

$$\Psi_3^2 \approx \frac{3C_3^2}{4}\left(\frac{12}{Re} + i\frac{4}{3}\right)\Phi_2^2 \quad \text{(F.23)}$$

with

$$|\Psi_3^2| \approx |\Im(\Psi_3^2)| \approx C_3^2|\Phi_2^2| = \sqrt{\frac{1}{7}}|\Phi_2^2|. \quad \text{(F.24)}$$

The dominant terms in the horizontal divergence Eq. (B.3) are

$$\left[\frac{6}{Re} + \frac{24\left(C_3^2\right)^2}{Re} + i\frac{24}{\epsilon}\right]\Phi_2^2 = \left[\frac{66}{7}\left(\frac{1}{Re}\right) + i\frac{24}{\epsilon}\right]\Phi_2^2 \approx \frac{-U_{2,E}^2}{\Omega}. \quad \text{(F.25)}$$

The resulting flow is given by

$$|\Phi_2^2| \approx |\Im(\Phi_2^2)| \approx \frac{\left|U_{2,E}^2\right|\epsilon}{24\Omega} = \frac{7}{8}\sqrt{\frac{2\pi}{15}}\frac{\Omega^3R^4e}{gh} \quad \text{(F.26)}$$

with

$$\Re\left(\Phi_2^2\right) \approx \frac{-U_{2,E}^2}{\Omega\left(\frac{24}{\epsilon}\right)^2}\left(\frac{66}{7}\left(\frac{1}{Re}\right)\right) = \frac{11}{8}\sqrt{\frac{2\pi}{15}}\left(\frac{\Omega^4R^4\nu e}{g^2h^2}\right). \quad \text{(F.27)}$$

Similar to (F.19), the average kinetic energy is

$$\begin{aligned} E_{tot,lib,E} &\approx \rho h\left[6|\Phi_2^2|^2 + 12\left(C_3^2|\Phi_2^2|\right)^2\right] = \rho h\left[\frac{54}{7}|\Phi_2^2|^2\right] \\ &\approx \frac{63\pi}{80}\frac{\rho\Omega^6R^8e^2}{g^2h} \end{aligned} \quad \text{(F.28)}$$

and the flow speed is

$$\bar{u} \approx \sqrt{\frac{63}{160}}\frac{\Omega^3R^3e}{gh} \quad \text{(F.29)}$$

Note that this value exceeds the equivalent westward flow speed (Eq. (F.20)), as expected. The corresponding energy dissipation for the eastward flow (28) is

$$\dot{E}_{lib,E} \approx -12\rho h U_{2,E}^2\Re\left(\Phi_{2,E}^2\right) \approx \frac{231\pi}{20}\frac{\rho\Omega^6R^6\nu e^2}{g^2h}. \quad \text{(F.30)}$$

The tidal quality factor is

$$Q_{lib,E} \approx \frac{\Omega\left(\frac{63\pi}{80}\frac{\rho\Omega^6R^8e^2}{g^2h}\right)}{\left(\frac{231\pi}{20}\frac{\rho\Omega^6R^6\nu e^2}{g^2h}\right)} = \frac{3}{44}\left(\frac{\Omega R^2}{\nu}\right) = \frac{3}{44}Re. \quad \text{(F.31)}$$

F.4. Scalings for the total response to the eccentricity tide

The three components of the eccentricity-driven flow behave quite similarly, and as seen in Appendices F.1, F.2 and F.3, the main difference exists in the pre-factors defining each of the flows. From (F.9), (F.19) and (F.28), the ratios of the kinetic energies are

$$E_{tot,lib,E} \approx \frac{147}{38}E_{tot,rad} \approx \frac{147}{5}E_{tot,lib,W} \quad \text{(F.32)}$$

with a total kinetic energy associated with the eccentricity tide of

$$E_{tot,ecc} \approx \frac{57\pi}{56}\frac{\rho\Omega^6R^8e^2}{g^2h}. \quad \text{(F.33)}$$

The energy dissipation behaves similarly with the eastward librational response contributing a bulk of the dissipation with non-negligible contributions from the other components. The relative dissipation rates from (F.12), (F.21) and (F.30) are

$$\dot{E}_{lib,E} \approx \frac{539}{130}\dot{E}_{rad} \approx \frac{539}{23}\dot{E}_{lib,W}. \quad \text{(F.34)}$$

The total energy dissipation associated with the eccentricity tide is

$$\dot{E}_{ecc,tot} \approx \frac{519\pi}{35}\frac{\rho\Omega^6 R^6 v e^2}{g^2 h}. \quad \text{(F.35)}$$

Thus, an approximation for Q related to all components of the eccentricity tide is

$$Q_{ecc} \approx \frac{\Omega\left(\frac{57\pi}{56}\frac{\rho\Omega^6 R^8 e^2}{g^2 h}\right)}{\frac{519\pi}{35}\frac{\rho\Omega^6 R^6 v e^2}{g^2 h}} = \frac{95}{1384}\left(\frac{\Omega R^2}{v}\right) = \frac{95}{1384}Re. \quad \text{(F.36)}$$

References

Agnor, C.B., Hamilton, D.P., 2006. Neptune's capture of its moon Triton in a binary-planetary gravitational encounter. Nature 441, 192–194.

Baines, P., 1973. The generation of internal tides by flat-bump topography. Deep Sea Res. 20, 179–205.

Baland, R., Yseboodt, M., Hoolst, T.V., 2012. Obliquity of the Galilean satellites: The influence of a global internal liquid layer. Icarus 220, 435–448.

Besserer, J., Nimmo, F., Roberts, J.H., Pappalardo, R.T., 2013. Convection-driven compaction as a possible origin of Enceladus's long wavelength topography. J. Geophys. Res. 118. http://dx.doi.org/10.1002/jgre.20079.

Beuthe, M., 2013. Spatial patterns of tidal heating. Icarus 223, 308–329.

Bills, B.G., 2005. Free and forced obliquities of the Galilean satellites of Jupiter. Icarus 175, 233–247.

Bills, B.G., Nimmo, F., 2008. Forced obliquity and moments of inertia of Titan. Icarus 196, 293–297.

Bills, B.G., Nimmo, F., 2011. Rotational dynamics and internal structure of Titan. Icarus 214, 351–355.

Bland, M.T., Showman, A.P., Tobie, G., 2009. The orbital–thermal evolution and global expansion of Ganymede. Icarus 199, 207–221.

Brito, D., Aurnou, J., Cardin, P., 2004. Turbulent viscosity measurements relevant to planetary core-mantle dynamics. Phys. Earth Planet. Inter. 141, 3–8.

Buffett, B.A., Christensen, U.R., 2007. Magnetic and viscous coupling at the core-mantle boundary: Inferences from observations of Earth's nutations. Geophys. J. Int. 171, 143–152.

Castillo-Rogez, J.C., Efroimsky, M., Lainey, V., 2011. The tidal history of Iapetus: Spin dynamics in the light of a refined dissipation model. J. Geophys. Res. 116. http://dx.doi.org/10.1029/2010JE004664.

Chen, E.M.A., Nimmo, F., 2011. Obliquity tides do not significantly heat Enceladus. Icarus 214, 779–781.

Chen, E.M.A., Glatzmaier, G.A., Nimmo, F., 2010. Modeling the dynamics of icy satellite sub-surface oceans with focus on implications for spacecraft observables. Lunar Planet. Sci. 41, 1454.

Colombo, G., 1966. Cassini's second and third laws. Astron. J. 71, 891–900.

Croft, S.K., Kargel, J.S., Kirk, R.L., Moore, J.M., Schenk, P.M., Strom, R.G., 1995. The geology of Triton. In: Cruikshank, D.P. (Ed.), Neptune and Triton. Univ. Arizona Press, pp. 879–947.

Darwin, G.H., 1899. The theory of the figure of the Earth carried to the second order of small quantities. Mon. Not. R. Astron. Soc. 60, 82–124.

Efroimsky, M., Williams, J.G., 2009. Tidal torques: A critical review of some techniques. Celest. Mech. Dyn. Astron. 104, 257–289.

Egbert, G.D., Ray, R.D., 2000. Significant dissipation of tidal energy in the deep ocean inferred from satellite altimeter data. Nature 405, 775–778.

Egbert, G.D., Ray, R.D., 2001. Estimates of M2 tidal energy dissipation from TOPEX/Poseidon altimeter data. J. Geophys. Res. 106, 22475–22502.

Ellsworth, K., Schubert, G., 1983. Saturn's icy satellites: Thermal and structural models. Icarus 54, 490–510.

Gaeman, J., Hier-Majumder, S., Roberts, J.H., 2012. Sustainability of a subsurface ocean within Triton's interior. Icarus 220, 339–347.

Garrick-Bethell, I., Nimmo, F., Wieczorek, M.A., 2010. Structure and formation of the lunar farside highlands. Science 330, 949–951.

Glatzmaier, G.A., 2002. Geodynamo simulations – How realistic are they? Annu. Rev. Earth Planet. Sci. 30, 237–257.

Goldreich, P., Soter, S., 1966. Q in the Solar System. Icarus 5, 375–389.

Goodman, J.C., Collins, G.C., Marshall, J., Pierrehumbert, R.T., 2004. Hydrothermal plume dynamics on Europa: Implications for chaos formation. J. Geophys. Res. 109. http://dx.doi.org/10.1029/2003JE002073.

Henning, W.G., O'Connell, R.J., Sasselov, D.D., 2009. Tidally heated terrestrial exoplanets: Viscoelastic response models. Astrophys. J. 707, 1000–1015.

Howett, C., Spencer, J.R., Pearl, J., Segura, M., 2011. High heat flow from Enceladus' south polar region measured using 10–600/cm Cassini/CIRS data. J. Geophys. Res. 116. http://dx.doi.org/10.1029/2010JE003718.

Hubbard, W.B., Anderson, J.D., 1978. Possible flyby measurements of Galilean satellite interior structure. Icarus 33, 336–341.

Hussmann, H., Spohn, T., 2004. Thermal–orbital evolution of Io and Europa. Icarus 171, 391–410.

Iess, L. et al., 2012. The tides of Titan. Science 337, 457–459.

Jacobson, R.A. et al., 2006. The gravity field of the saturnian system from satellite observations and spacecraft tracking data. Astron. J. 132, 2520–2526.

Jacobson, R.A., 2009. The orbits of the Neptunian satellites and the orientation of the pole of Neptune. Astron. J. 137, 4322–4329.

Jacobson, R.A., Campbell, J.K., Taylor, A., Synott, S.P., 1992. The masses of Uranus and its major satellites from Voyager tracking data and Earth-based Uranian satellite data. Astron. J. 103, 2068–2078.

Jankowski, D.G., Chyba, C.F., Nicholson, P.D., 1989. On the obliquity and tidal heating of Triton. Icarus 80, 211–219.

Jayne, S.R., Laurent, L.C.S., 2001. Paramterizing tidal dissipation over rough topography. Geophys. Res. Lett. 28, 211–219.

Jeffreys, H., 1921. Tidal friction in shallow seas. Phil. Trans. R. Soc. A 221, 239–264.

Kargel, J.S., Kaye, J.Z., Head, J.W., Marion, G.M., Sassen, R., Crowley, J.K., Ballesteros, O.P., Grant, S.A., Hogenboom, D.L., 2000. Europa's crust and ocean: Origin, composition, and the prospects for life. Icarus 148, 226–265.

Kaula, W.M., 1964. Tidal dissipation by solid friction and the resulting orbital evolution. Rev. Geophys. 2, 661–685.

Khurana, K.K. et al., 1998. Induced magnetic fields as evidence for subsurface oceans in Europa and Callisto. Nature 395, 777–780.

Kivelson, M.G., Khurana, K., Volwerk, M., 2002. The permanent and inductive magnetic moments of Ganymede. Icarus 157, 507–522.

Longuet-Higgins, M., 1968. The eigenfunctions of Laplace's tidal equations over a sphere. Phil. Trans. R. Soc. A 262, 511–607.

Love, A.E.H., 1944. A Treatise on the Mathematical Theory of Elasticity. Dover.

Lumb, L.I., Aldridge, K.D., 1991. On viscosity estimates for the Earth's fluid outer core and core-mantle coupling. J. Geomag. Geoelectr. 43, 93–110.

Matsuyama, I., 2012. Tidal dissipation in the subsurface oceans of icy satellites. Lunar Planet. Sci. 43, 2068.

McKinnon, W.B., Kirk, R.L., 2007. Triton. In: McFadden, L.-A., Weissman, P.R., Johnson, T.V. (Eds.), Encyclopedia of the Solar System. Academic Press, pp. 483–502.

Meyer, J., Wisdom, J., 2007. Tidal heating in Enceladus. Icarus 188, 535–539.

Meyer, J., Elkins-Tanton, L., Wisdom, J., 2010. Coupled thermal–orbital evolution of the early Moon. Icarus 208, 1–10.

Mound, J., Buffett, B., 2007. Viscosity of the Earth's fluid core and torsional oscillations. J. Geophys. Res. 112. http://dx.doi.org/10.1029/2006JB004426.

Munk, W.H., MacDonald, G.J.F., 1960. The Rotation of the Earth: A Geophysical Discussion. Cambridge Univ. Press.

Murray, C.D., Dermott, S.F., 1999. Solar System Dynamics. Cambridge Univ. Press.

Nimmo, F., Bills, B.G., 2010. Shell thickness variations and the long-wavelength topography of Titan. Icarus 208, 896–904.

Nimmo, F., Gaidos, E., 2002. Strike-slip motion and double ridge formation on Europa. J. Geophys. Res. 107. http://dx.doi.org/10.1029/2000JE001476.

Nimmo, F., Faul, U.H., Garnero, E.J., 2012. Dissipation at tidal and seismic frequencies in a melt-free Moon. J. Geophys. Res. 117. http://dx.doi.org/10.1029/2012JE004160.

Ogilvie, G.I., Lin, D.N.C., 2004. Tidal dissipation in rotating giant planets. Astrophys. J. 610, 477–509.

Ojakangas, G.W., Stevenson, D.J., 1989. Thermal state of an ice shell on Europa. Icarus 81, 220–241.

Peale, S.J., 1969. Generalized Cassini's laws. Astron. J. 74, 483–489.

Peale, S.J., Cassen, P., 1978. Contributions of tidal dissipation to lunar thermal history. Icarus 36, 245–269.

Peale, S.J., Cassen, P., Reynolds, R.T., 1979. Melting of Io by tidal dissipation. Science 203, 892–894.

Pope, S.B., 2000. Turbulent Flows. Cambridge Univ. Press.

Postberg, F., Schmidt, J., Hillier, J., Kempf, S., Srama, R., 2011. A salt-water reservoir as the source of a compositionally stratified plume on Enceladus. Nature 474, 620–622.

Prockter, L.M., Nimmo, F., Pappalardo, R.T., 2005. A shear heating origin for ridges on Triton. Geophys. Res. Lett. 32. http://dx.doi.org/10.1029/2005GL0022832.

Radau, R., 1885. Sur la loi des densites a l'interieur de la terre. Compt. Rend. 100, 972–974.

Ray, R., Eanes, R.J., Lemoine, F.G., 2001. Constraints on energy dissipation in the Earth's body tide from satellite tracking and altimetry. Geophys. J. Int. 144, 471–480.

Roberts, J.H., Nimmo, F., 2008. Tidal heating and the long-term stability of a subsurface ocean on Enceladus. Icarus 194, 675–689.

Ross, M.N., Schubert, G., 1989. Viscoelastic models of tidal heating on Enceladus. Icarus 78, 90–101.

Ross, M.N., Schubert, G., 1990. The coupled orbital and thermal evolution of Triton. Geophys. Res. Lett. 17, 1749–1752.

Schenk, P.M., McKinnon, W.B., 2009. One-hundred-km-scale basins on Enceladus: Evidence for an active ice shell. Geophys. Res. Lett. 26. http://dx.doi.org/10.1029/2009GL039916.

Schenk, P.M., Zahnle, K., 2007. On the negligible surface age of Triton. Icarus 192, 135–149.

Schubert, G., Anderson, J.D., Spohn, T., McKinnon, W.B., 2004. Interior composition, structure and dynamics of the Galilean satellites. In: Bagenal, F., Dowling, T., McKinnon, W. (Eds.), Jupiter: The Planet, Satellites and Magnetosphere. Cambridge Univ. Press, pp. 281–306.

Segatz, M., Spohn, T., Ross, M., Schubert, G., 1988. Tidal dissipation, surface heat flow, and figure of viscoelastic models of Io. Icarus 75, 187–206.

Showman, A.P., Stevenson, D.J., Malhotra, R., 1997. Coupled orbital and thermal evolution of Ganymede. Icarus 129, 367–383.

Smith, B.A. et al., 1989. Voyager 2 at Neptune: Imaging science results. Science 246, 1422–1449.

Smylie, D., 1999. Viscosity near Earth's solid inner core. Science 284, 461–463.

Soderlund, K.M., Schmidt, B.E., Blankenship, D.E., Wicht, J., 2013. Dynamics of Europa's ocean and sensitivity to water properties. Lunar Planet. Sci. 44, 3009.

Sohl, F., Sears, W.D., Lorenz, R.D., 1995. Tidal dissipation on Titan. Icarus 115, 278–294.
Spencer, J.R. et al., 2006. Cassini encounters Enceladus: Background and the discovery of a south polar hot spot. Science 311, 1401–1405.
Squyres, S.W., Reynolds, R.T., Cassen, P.M., Peale, S.J., 1983. The evolution of Enceladus. Icarus 53, 319–331.
Stiles, B.W. et al., 2008. Determining Titan's spin state from Cassini RADAR images. Astron. J. 135, 1669–1680.
Tackley, P.J., Schubert, G., Glatzmaier, G.A., Schenk, P., Ratcliff, J.T., Matas, J., 2001. Three-dimensional simulations of mantle convection in Io. Icarus 149, 79–93.
Taylor, G.I., 1920. Tidal friction in the Irish Sea. Phil. Trans. R. Soc. A 220, 1–33.
Thomas, P.C., 1988. Radii, shapes and topography of the satellites of Uranus from limb coordinates. Icarus 73, 427–441.
Thomas, P.C., 2000. The shape of Triton from limb profiles. Icarus 148, 587–588.
Thomas, P.C., 2010. Sizes, shapes, and derived properties of the saturnian satellites after the Cassini nominal mission. Icarus 208, 395–401.
Tobie, G., Mocquet, A., Sotin, C., 2005. Tidal dissipation within large icy satellites: Applications to Europa and Titan. Icarus 177, 534–549.
Tyler, R.H., 2008. Strong ocean tidal flow and heating on moons of the outer planets. Nature 456, 770–772.
Tyler, R.H., 2009. Ocean tides heat Enceladus. Geophys. Res. Lett. 36. http://dx.doi.org/10.1029/2009GL038300.
Tyler, R., 2011. Tidal dynamical considerations constrain the state of an ocean on Enceladus. Icarus 211, 770–779.
Ward, W.R., 1975. Past orientation of the lunar spin axis. Science 189, 377–379.
Wisdom, J., 2004. Spin–orbit secondar resonance dynamics of Enceladus. Astron. J. 128, 484–491.
Wisdom, J., 2008. Tidal dissipation at arbitrary eccentricity and obliquity. Icarus 193, 637–640.
Zebker, H.A., Stiles, B., Hensley, S., Lorenz, R., Kirk, R.L., Lunine, J., 2009. Size and shape of Saturn's moon Titan. Science 324, 921–923.
Zhang, K., Nimmo, F., 2012. Late-stage impacts and the orbital and thermal evolution of Tethys. Icarus 218, 348–355.